Geochemistry, Geophysics, Geosystems

RESEARCH ARTICLE
10.1029/2018GC008126

Special Section:
Polar region geosystems

Subglacial Geology and Geomorphology of the Pensacola-Pole Basin, East Antarctica

Guy J. G. Paxman[1], Stewart S. R. Jamieson[1], Fausto Ferraccioli[2], Tom A. Jordan[2], Michael J. Bentley[1], Neil Ross[3], René Forsberg[4], Kenichi Matsuoka[5], Daniel Steinhage[6], Graeme Eagles[6], and Tania G. Casal[7]

[1]Department of Geography, Durham University, Durham, UK, [2]British Antarctic Survey, Cambridge, UK, [3]School of Geography, Politics and Sociology, Newcastle University, Newcastle upon Tyne, UK, [4]Geodynamics, National Space Institute, Technical University of Denmark, Lyngby, Denmark, [5]Norwegian Polar Institute, Tromsø, Norway, [6]Alfred Wegener Institute Helmholtz Centre for Polar and Marine Research, Bremerhaven, Germany, [7]European Space Agency/ESTEC, Noordwijk, Netherlands

Abstract The East Antarctic Ice Sheet (EAIS) is underlain by a series of low-lying subglacial sedimentary basins. The extent, geology, and basal topography of these sedimentary basins are important boundary conditions governing the dynamics of the overlying ice sheet. This is particularly pertinent for basins close to the grounding line wherein the EAIS is grounded below sea level and therefore potentially vulnerable to rapid retreat. Here we analyze newly acquired airborne geophysical data over the Pensacola-Pole Basin (PPB), a previously unexplored sector of the EAIS. Using a combination of gravity and magnetic and ice-penetrating radar data, we present the first detailed subglacial sedimentary basin model for the PPB. Radar data reveal that the PPB is defined by a topographic depression situated ~500 m below sea level. Gravity and magnetic depth-to-source modeling indicate that the southern part of the basin is underlain by a sedimentary succession 2–3 km thick. This is interpreted as an equivalent of the Beacon Supergroup and associated Ferrar dolerites that are exposed along the margin of East Antarctica. However, we find that similar rocks appear to be largely absent from the northern part of the basin, close to the present-day grounding line. In addition, the eastern margin of the basin is characterized by a major geological boundary and a system of overdeepened subglacial troughs. We suggest that these characteristics of the basin may reflect the behavior of past ice sheets and/or exert an influence on the present-day dynamics of the overlying EAIS.

Key Points:
- We present new compilations of ice thickness, bedrock topography, and gravity anomalies for the Pensacola-Pole Basin
- A significant sedimentary succession, 2–3 km in thickness, is preserved beneath the southern part of the basin
- Basin topography and geology may have influenced the dynamics of past and present-day ice sheets

Supporting Information:
- Supporting Information S1

Correspondence to:
G. J. G. Paxman,
guy.j.paxman@durham.ac.uk

Citation:
Paxman, G. J. G., Jamieson, S. S. R., Ferraccioli, F., Jordan, T. A., Bentley, M. J., Ross, N., et al. (2019). Subglacial geology and geomorphology of the Pensacola-Pole Basin, East Antarctica. *Geochemistry, Geophysics, Geosystems*, *20*, 2786–2807. https://doi.org/10.1029/2018GC008126

Received 15 JAN 2019
Accepted 20 MAY 2019
Accepted article online 28 MAY 2019
Published online 19 JUN 2019

1. Introduction

Low-lying subglacial topography across West Antarctica and around large tracts of the margin of East Antarctica is hypothesized to render the overlying sectors of the Antarctic Ice Sheet vulnerable to rapid retreat or even catastrophic collapse in a warming world (Mercer, 1978; Schoof, 2003; Thomas, 1979). In addition, the presence of deformable sediment within topographic basins beneath the West Antarctic Ice Sheet is thought to influence ice sheet dynamics by promoting streaming flow (Anandakrishnan et al., 1998; Bell et al., 1998; Studinger et al., 2001). Recent numerical ice sheet simulations indicate that the majority of East Antarctic Ice Sheet (EAIS) retreat in the near-future will be focused within the Wilkes, Recovery and Aurora Subglacial Basins (DeConto & Pollard, 2016; Golledge et al., 2017, 2015; Mengel & Levermann, 2014; Pollard et al., 2015), from which ice mass loss will potentially contribute 9–15 m of sea level rise in a warming world (Gasson et al., 2015).

Exploration of these basins using airborne geophysics has brought about increased understanding of their extent, subglacial topography, geology, and tectonic architecture (Aitken et al., 2016; Diez et al., 2018; Ferraccioli et al., 2009; Frederick et al., 2016; Maritati et al., 2016; Paxman et al., 2017; Ross et al., 2012). These parameters lead to improved understanding of the tectonic and surface processes responsible for shaping the modern-day topography of subglacial East Antarctica, and in turn the dynamics of the overlying EAIS. Hence, characterization of subglacial basins has the potential to improve future ice sheet projections and can also inform models of EAIS dynamics in past warmer climates (Aitken et al., 2016; Paxman et al., 2018; Young et al., 2011), which may represent an analog for a future warmer world.

The presence of a deep subglacial basin extending from the southeastern Weddell Sea to the South Pole has been hypothesized since the 1980s (Drewry, 1983), but until recently, this part of Antarctica remained

largely unexplored, with very few direct ice thickness measurements (~5,000 line-km) included in the Bedmap2 compilation (Fretwell et al., 2013). Consequently, the region has been highlighted as one of high uncertainty in ice sheet models and future sea level rise predictions (Gasson et al., 2015). In 2015–2016, the European Space Agency PolarGAP project (Jordan et al., 2018; Winter et al., 2018) collected >38,000 line-km of new aerogeophysical data around South Pole (Figure 1a). The primary focus of this survey was collecting airborne gravity data to fill the polar gap in both satellite and existing airborne gravity coverage south of 83.5°S (Scheinert et al., 2016). In addition, airborne radio-echo sounding (RES) and magnetic data were acquired to improve understanding of the subglacial landscape and geology around South Pole. These aerogeophysical data sets confirmed the presence of a large subglacial depression known as the Pensacola-Pole Basin (PPB), extending from the grounding line near the Pensacola Mountains to the South Pole (Jordan et al., 2018).

By analogy with similar subglacial basins around the East Antarctic margin, the PPB is a potential locus of significant EAIS retreat under warmer climate scenarios. The basin is overlain by the fast-flowing Support Force and Academy Glaciers, which drain into the Ronne-Filchner Ice Shelf (Figure 1b; Bingham et al., 2007; Rignot et al., 2011), which may become unstable in a warming world (Bingham et al., 2015; Hellmer et al., 2012; Ross et al., 2012). Ice shelf collapse has been shown to directly lead to glacier acceleration and thinning, causing sea level rise (Scambos et al., 2004), and numerical models indicate that mass flux across the grounding line at the Support Force and Academy Glaciers is particularly sensitive to ice shelf mass (Reese et al., 2018). Ice sheet simulations indicate that the ice stored in the PPB and surrounding catchment could contribute up to 2 m of sea level rise in a warmer climate, although there is large uncertainty due to poorly constrained bedrock elevations in the Bedmap2 data set (Gasson et al., 2015). The aim of this study is to use airborne geophysical data sets to characterize the PPB by constraining the subglacial topography and geology of the basin and surrounding regions. In so doing we aim to examine the relationship between basal conditions and the dynamics of the overlying EAIS and facilitate improved ice sheet models for this catchment.

2. Regional Geological Setting

The PPB is surrounded by highlands, including (starting from grid north and moving clockwise around the South Pole) the Polargap Subglacial Highlands, Recovery Subglacial Highlands, southern Transantarctic Mountains (TAM), Thiel Mountains, and Pensacola Mountains (Patuxent, Neptune, Forrestal, and Argentina Ranges). The southern TAM, Thiel Mountains, and Pensacola Mountains protrude above the EAIS as nunataks, and bedrock is also exposed in the Whichaway Nunataks, Shackleton Range, and Theron Mountains to the northeast of the PPB. The geology of the southern TAM (Figure 2c) comprises a Neoproterozoic–Cambrian metasedimentary basement complex; these rocks were deformed during the Cambro–Ordovician Ross Orogeny (Storey et al., 1996), at which time the granites/granodiorites of the Granite Harbour Intrusives were emplaced (Stump, 1995). The basement rocks were truncated to form the Kukri Peneplain, a widespread erosion surface upon which Devonian–Triassic alluvial, fluvial, glacial, and shallow-marine sediments of the Beacon Supergroup were deposited (Barrett, 1991). The Beacon strata are intruded and overlain by Jurassic dolerites associated with the Ferrar Large Igneous Province (Elliot & Fleming, 2004).

The Pensacola and Thiel Mountains are made up of a Neoproterozoic and Cambrian phyllitic metasedimentary sequence (Figure 2a), including interbedded greywacke slates, limestones (Evans et al., 2018), sandstones, and shales, as well as Cambro–Ordovician granites, rhyolites, and quartz monzonite porphyries (Schmidt & Ford, 1969). In the Pensacola Mountains, Ordovician–Silurian terrestrial sandstones and conglomerates are also exposed (Schmidt & Ford, 1969). Here the Kukri Peneplain is represented by a nonconformity or angular unconformity, above which lie Devonian–Permian limestones, sandstones, siltstones, mudstones, and shales, which are thought to be equivalent to the Beacon Supergroup in the southern TAM (Schmidt & Ford, 1969). These rocks are intruded by Jurassic Ferrar dolerite sills, which are exposed at Lewis Nunatak and along the Pecora Escarpment (Figure 2a). This Jurassic episode of magmatism is also represented by the extensive layered gabbro intrusion of the Dufek Massif (Ferris et al., 1998).

The Shackleton Range likewise dominantly comprises Neoproterozoic–Cambrian basement rocks, with small isolated outcrops of younger Paleozoic sediments (Figure 2b; Tessensohn et al., 1999). The

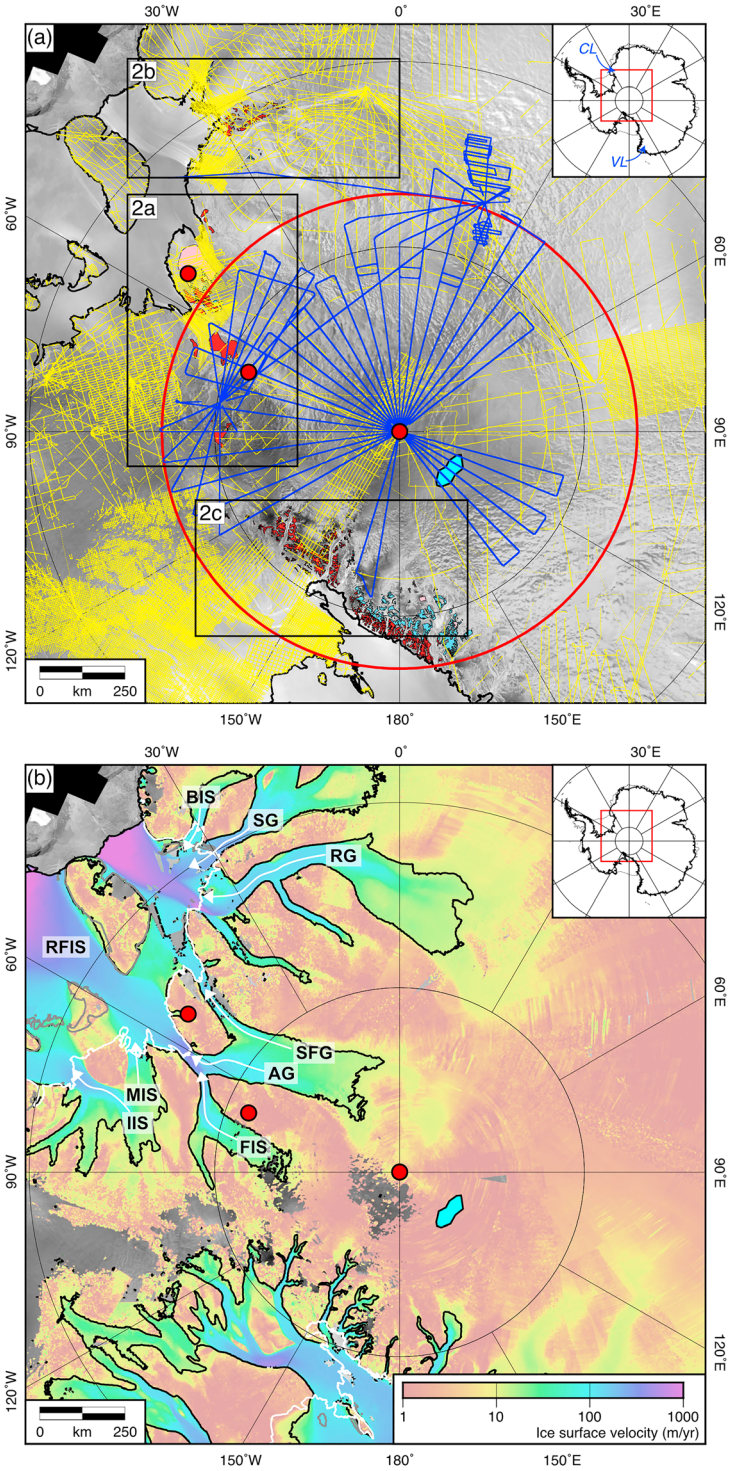

Figure 1. Regional setting. (a) Airborne geophysical data coverage over the South Pole region. Blue radial lines indicate paths flown during the 2015–2016 PolarGAP survey, which was used to fill the gap in satellite gravity coverage south of 83.5°S (red circle). Yellow lines show flight lines from other aerogeophysical surveys. Colored polygons denote rock outcrops (Figure 2). Filled red circles show the location of seismic stations. Light blue polygon shows the location of a geothermal heat flux anomaly near South Pole (Jordan et al., 2018). Inset shows the study region within Antarctica (CL = Coats Land; VL = Victoria Land). (b) Ice surface velocity (Rignot et al., 2011). The 20 m/year ice surface velocity contour (black line) is used to outline regions of enhanced ice flow. The white line marks the grounding line, black line marks the outer ice shelf edge, and gray lines mark islands. White arrows show major glacier outlets that flow into the Weddell Sea. AG = Academy Glacier; BIS = Bailey Ice Stream; FIS = Foundation Ice Stream; IIS = Institute Ice Stream; MIS = Möller Ice Stream; SFG = Support Force Glacier; SG = Slessor Glacier; RFIS = Ronne-Filchner Ice Shelf; RG = Recovery Glacier. All figures and grids in this manuscript are displayed in Polar Stereographic projection with true scale at 71°S (EPSG3031).

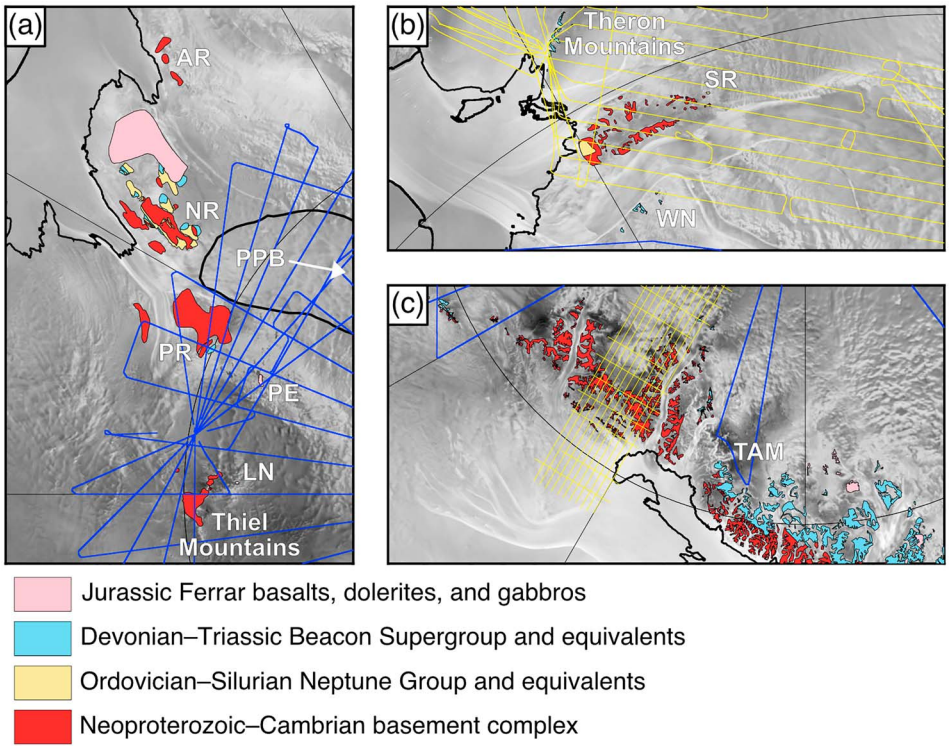

Figure 2. Geology of the study region. (a) Simplified outcrop geology of the Pensacola and Thiel Mountains. Abbreviations: AR = Argentina Range; PPB = Pensacola-Pole Basin (outlined in black); NR = Neptune Range; PR = Patuxent Range; PE = Pecora Escarpment; LN = Lewis Nunataks. (b) Simplified outcrop geology of the Shackleton Range and Theron Mountains. Abbreviations: SR = Shackleton Range; WN = Whichaway Nunataks. (c) Simplified outcrop geology of the southern Transantarctic Mountains (TAM). Note that areas mapped as comprising Beacon Supergroup rocks may also contain sills of Ferrar dolerite. The locations of panels a, b and c are shown in Figure 1a. Locations of flight lines used in this study are shown in each panel (blue lines indicate PolarGAP flights; yellow lines indicate previous surveys). Simplified outcrop geology is sourced from American Geographical Society Folio 12 Antarctic geology maps and other regional studies (McGregor & Wade, 1969; Mirsky, 1969; Schmidt & Ford, 1969; Tessensohn et al., 1999).

mountains are hypothesized to represent an uplifted basement horst block bounded by faults that trend parallel to the Recovery and Slessor Glaciers (Paxman et al., 2017). Rock outcrops in the Theron Mountains and Whichaway Nunataks are represented by Beacon Supergroup strata and Ferrar dolerites (Brook, 1972).

3. Methods

3.1. Subglacial Topography Characterization

The large-scale geomorphology of Antarctica's subglacial topography is an important repository of information relating to geology and past processes of landscape evolution (Aitken et al., 2016; Jamieson et al., 2014; Paxman et al., 2018; Young et al., 2011). Antarctic ice thickness and bedrock elevation are determined using (predominantly airborne) RES surveys. In order to produce an updated ice thickness grid and bedrock digital elevation model (DEM) for the South Pole region, it was necessary to compile ice thickness measurements from a number of airborne geophysical campaigns, including PolarGAP (Jordan et al., 2018; Winter et al., 2018), FISS, RECISL (Humbert et al., 2018), ICEGRAV (Forsberg et al., 2018; Paxman et al., 2017), IMAFI (Jeofry et al., 2018; Ross et al., 2012), ICECAP (Blankenship et al., 2017), AGAP (Bell et al., 2011), Operation IceBridge (Leuschen et al., 2016), AFI-Coats Land (Bamber et al., 2006), PPT (Studinger et al., 2006), DUFEK (Ferris et al., 2003), CASERTZ (Bell et al., 1998), and SPRI-NSF-TUD (Drewry, 1983). Detailed information on the acquisition and processing of the RES data from each survey can be found in the respective references listed above.

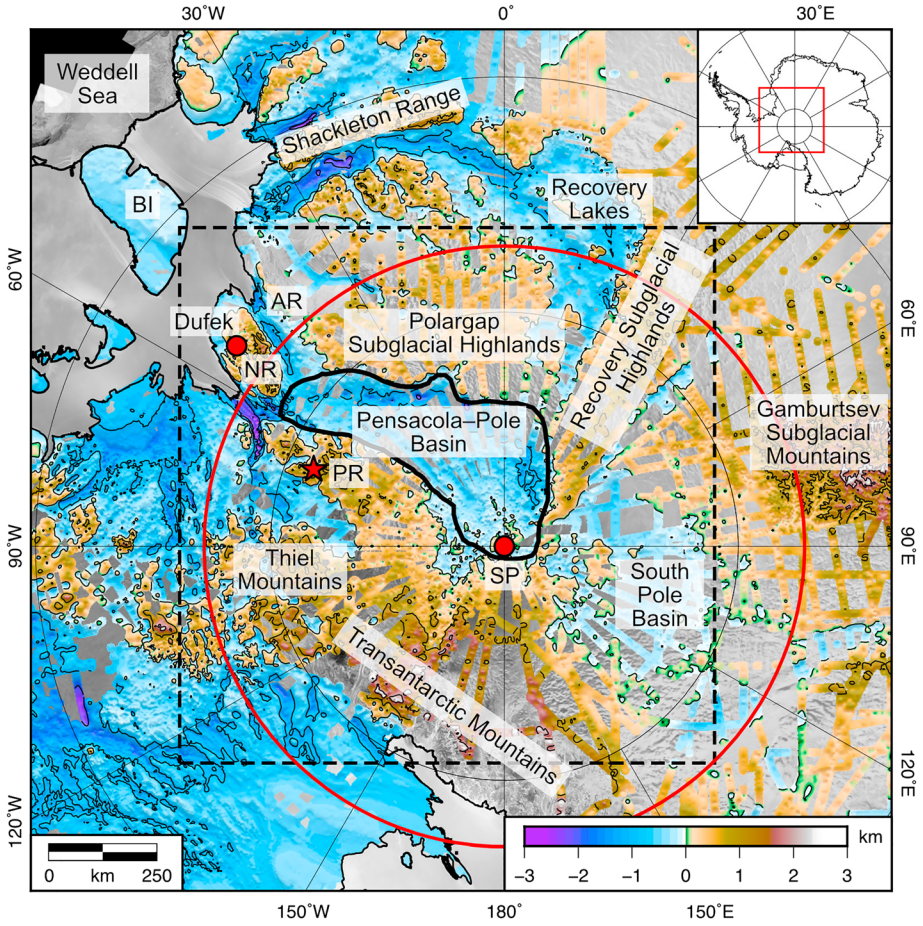

Figure 3. New bedrock topography digital elevation model of the South Pole region. Bedrock elevations are contoured at 1 km intervals. Black polygon shows the outline of the Pensacola-Pole Basin. Filled red circles show the location of seismic stations. Red star marks the Pecora Escarpment, where Ferrar dolerites are exposed (and a seismic station is also present). Major topographic features are labeled. Abbreviations: BI = Berkner Island; AR = Argentina Range; NR = Neptune Range; PR = Patuxent Range; SSouth Pole. Black dashed box shows the main study area, which defines the extent of subsequent figures. Red circle marks the polar gap south of 83.5°S. Inset shows the study region within Antarctica.

We assembled all available ice thickness point data from each survey and merged these into a single database. Crossover analysis (independent measurements of ice thickness at the same position) yielded a standard deviation of 57.7 m at line intersections, with no systematic line-to-line biases. This value is skewed by a relatively small number of high crossover misfits over rough topography, where the bed elevation is more difficult to determine. We used a recently updated ice surface DEM derived from CryoSat-2 satellite radar altimeter measurements (Slater et al., 2018). The satellite surface elevation data coverage contains a gap south of 88°S, which we filled with laser- and RES-derived surface elevation data from the relevant airborne surveys listed above. The ice thickness point data were then subtracted from the ice surface elevation and interpolated onto a 2.5 km grid mesh using a continuous curvature spline algorithm with a tension factor of 0.35, an appropriate value for steep topography data (Wessel et al., 2013). The resulting bedrock topography DEM (Figure 3) was masked to remove any interpolated values more than 10 km from the nearest data point. The surface (Figure 4a) and bedrock elevations were referenced to the GL04C geoid, as is used in Bedmap2 (Fretwell et al., 2013). The difference between our new bedrock topography DEM and Bedmap2 shows good agreement where the same data were used in both grids but significant differences where new data sets have been included (see Figure S1 in the supporting information).

Along certain sections of some PolarGAP flight lines, the bed reflection is not clearly imaged by RES, likely due to the attenuation of radar energy in (warm) ice >3 km thick, due to steep bedrock topography, and/or due to a lack of a distinct interface between ice and the underlying material. Other surveys such as Operation

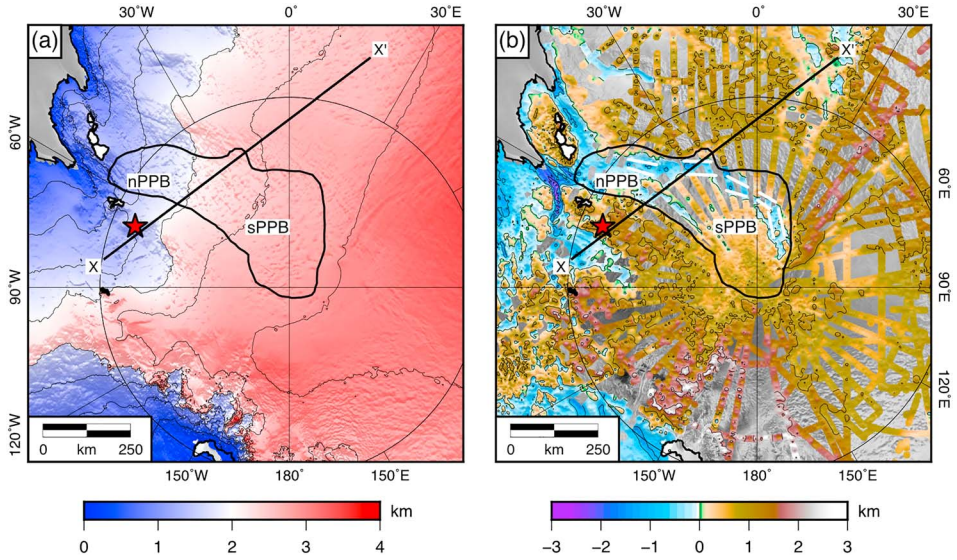

Figure 4. (a) Surface elevation (Slater et al., 2018). (b) Bedrock elevation, isostatically rebounded for the removal of the present-day ice load. White lines mark the outlines of overdeepened graben-like features trending along the eastern margin of the Pensacola-Pole Basin (PPB). In each panel, the black polygon shows the outline of the PPB. Red star marks the Pecora Escarpment, where Ferrar dolerites are exposed. White filled polygons outline plateau surfaces outcropping in the mountain ranges surrounding the PPB. The northern (nPPB) and southern (sPPB) regions of the basin, as described in the text, are indicated. Profile X–X′ is shown in Figure 6.

IceBridge and PPT, which carry different radar platforms (Leuschen et al., 2016; Studinger et al., 2006), also show data gaps in the same places. Within the PPB, these gaps most likely indicate areas where the bed is particularly deep; corresponding gravity anomaly "lows" support this interpretation. While the continuous curvature gridding algorithm can be expected to interpolate the locations of these deep areas, the gravity data offer an independent constraint on their depth. To profit from this, we inverted the gravity anomaly data to estimate the bedrock elevation along sections of the profiles not imaged by RES (see Figure S2 in the supporting information), under the assumption that the gravity anomalies solely reflect the subglacial topography and not bedrock density variations. Where no radar picks were available, we included these inverted bedrock elevations in our bedrock DEM.

As well as providing a boundary condition for ice sheet models, our new bed DEM forms the basis for characterizing the subglacial topography of the PPB and surrounding areas. The original radargrams and bed picks were also used to aid mapping and interpretation of macroscale geomorphological features within the subglacial landscape. The elevation of the bed under ice-free conditions is also of interest for assessing the roles of preglacial erosional and depositional processes. We used a flexural isostatic model (see section 3.2.1) to rebound our bedrock DEM for the removal of the modern ice load (assuming ice and mantle densities of 920 and 3,330 kg/m^3 respectively; see Figure S3 in the supporting information). This rebounded DEM (Figure 4b) gives an indication of the preglacial elevation of the basin, although we note that glacial erosion and the associated isostatic responses have likely also driven vertical topographic displacement since 34 Ma (Paxman et al., 2016).

3.2. Basin Thickness Modeling

In this section, we describe several methods used to determine the thickness of sedimentary rocks within the PPB from gravity and magnetic data.

3.2.1. Gravity Modeling

We assembled gravity line data from relevant surveys in order to produce an updated gravity anomaly map of the South Pole region. The profile data were upward or downward continued to a constant altitude of 3,400 m above the Bedmap2 geoid, to compensate for differences in flight elevations. Downward continuation can introduce high-frequency artifacts, which we removed using a 10 km low-pass filter in recognition of the fact that the filtering required to smooth aircraft accelerations limits the shortest resolvable wavelength of the FAA to ~9 km. Remaining systematic biases between the surveys were accounted for by leveling the data,

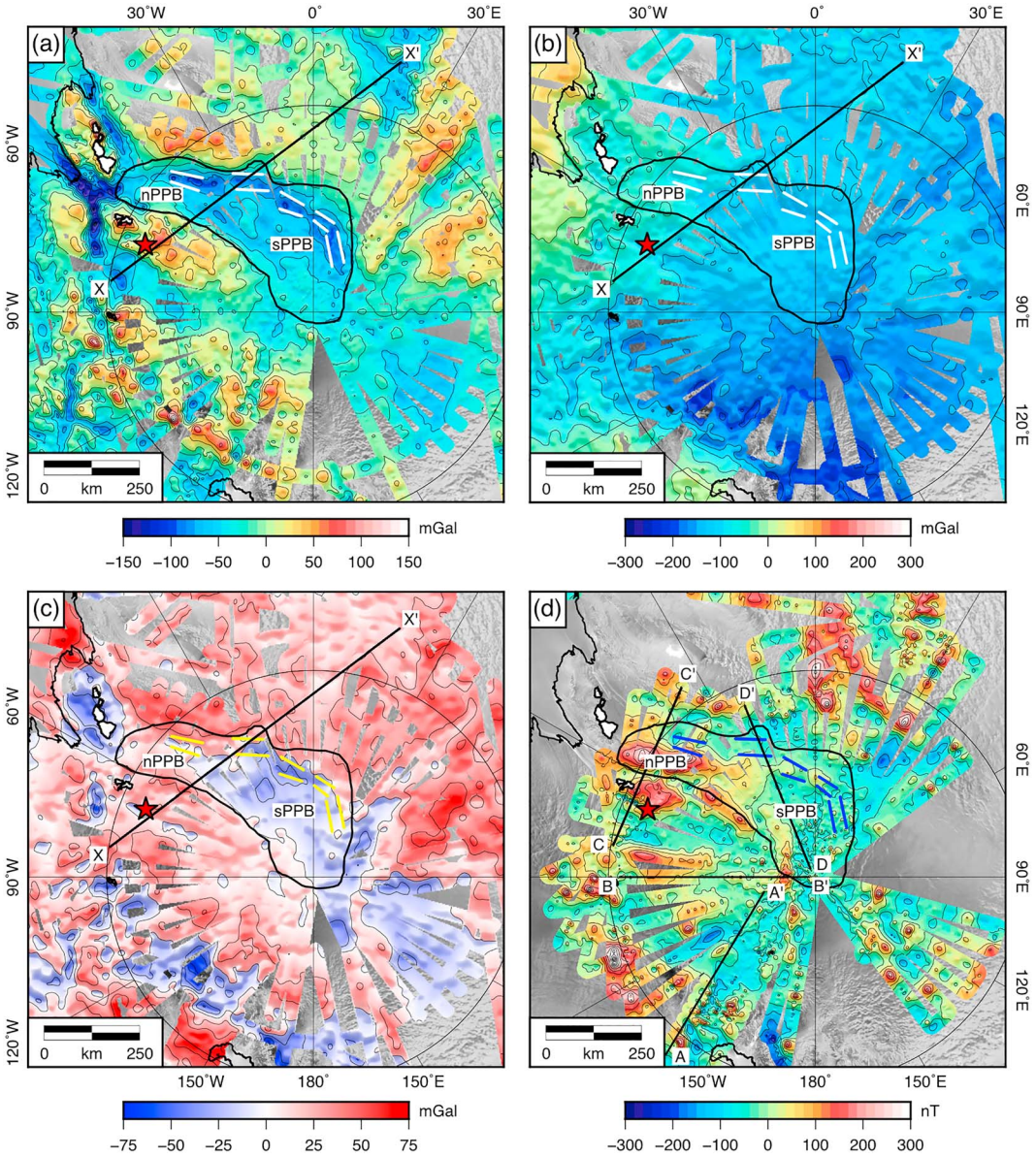

Figure 5. Gravity and magnetic anomalies in the South Pole region. (a) Free-air anomaly compilation contoured at 25 mGal intervals. Gravity anomalies from multiple airborne surveys are merged and leveled and upward continued to 3,400 m above the geoid. (b) Bouguer anomaly at 3,400 m above the geoid contoured at 50 mGal intervals. (c) Flexural isostatic anomaly (T_e = 30 km) at 3,400 m above the geoid contoured at 25 mGal intervals. (d) Magnetic anomaly contoured at 50 nT intervals. Black polygon shows the outline of the Pensacola-Pole Basin (PPB). Red star marks the Pecora Escarpment, where Ferrar dolerites are exposed. White filled polygons outline plateau surfaces outcropping in the mountain ranges surrounding the PPB. Colored lines (white in panels a and b, yellow in panel c, and blue in panel d) mark the outlines of overdeepened graben-like features trending along the eastern margin of the PPB. The northern (nPPB) and southern (sPPB) regions of the basin, as described in the text, are indicated. Profile X–X′ is presented in Figure 6.

after which the root mean square crossover error between all flight intersections was reduced to ~5 mGal. The leveled free-air anomaly (FAA) data were then gridded together at 2.5 km horizontal resolution using a continuous curvature spline with a tension factor of 0.3, an appropriate value for potential field data (Wessel et al., 2013; Figure 5a).

We computed a Bouguer correction incorporating the gravity effects of our ice surface and bedrock topography DEMs (section 3.1). For each surface, we used Parker's fast Fourier transform (FFT) method for determining the gravity effect of an undulating topographic interface with a uniform density contrast, assuming typical densities of 0, 920, and 2670 kg/m^3 for air, ice, and rock, respectively (Parker, 1972). Each correction was calculated at an altitude of 3,400 m above the geoid and then summed to give a total Bouguer correction.

The total Bouguer correction was filtered with a 9 km half-wavelength Gaussian filter to match the resolution of the FAA and then subtracted from the FAA to yield a Bouguer anomaly (Figure 5b). We determined an isostatic gravity correction using a flexural model to define the Moho. The flexural model used an effective elastic thickness (T_e) of 30 km, reflecting a realistic average for lithosphere near the boundary between West and East Antarctica (Paxman et al., 2017; Studinger & Miller, 1999). The absolute modeled Moho depth was tied to estimates from teleseismic receiver functions made at three seismic stations surrounding the PPB (Chaput et al., 2014; Winberry & Anandakrishnan, 2004). The flexural isostatic correction was computed at 3,400 m above the geoid and subtracted from the Bouguer anomaly to yield a flexural isostatic anomaly (Figure 5c).

We used 2-D forward gravity modeling to estimate the thickness of any potential sedimentary succession within the PPB. This method has been previously applied to constrain sediment thickness in regions of Antarctica lacking active-source seismic reflection data (Aitken et al., 2016; Studinger et al., 2004). For each PolarGAP flight line crossing the PPB, we set up an initial model comprising three layers: ice sheet, crust, and mantle, for which we assumed uniform densities of 920, 2,670, and 3,300 kg/m^3, respectively. The ice surface and bedrock interfaces were taken from the laser/RES line data, and the Moho was defined using the flexural model described in the previous paragraph.

The gravity effects of the ice surface, ice bed, and Moho density interfaces were computed using a FFT (Parker, 1972), summed, and compared to the observed FAA. Before forward modeling, the observed FAA was filtered to remove the long wavelength (>1,200 km) signal, which reflects mantle dynamics rather than plate processes such as flexural isostasy (Watts & Moore, 2017). Where the modeled gravity anomaly was consistently more positive than the observed anomaly, we introduced a fourth layer representing low-density sedimentary rocks, with a density of 2,400 kg/m^3. We forward modeled the geometry of the sediment layer to minimize the misfit between the observed and modeled FAA. The resulting model provides an estimate of the 2-D geometry of the sedimentary basin along the profile. We interpolated the modeled sediment thickness across all lines (see Figures S4 and S5 in the supporting information) using a tensional spline (Wessel et al., 2013) to produce a 3-D sediment thickness map for the PPB.

Forward gravity models are nonunique, and it is therefore important to quantify the uncertainty associated with the resulting estimate of sediment thickness. We determined the uncertainty in sediment thickness associated with a reasonable range of sediment densities (2,250–2,550 kg/m^3) and elastic thicknesses used in the isostatic model of the Moho (10–50 km). In sections of the profile where the bed is not imaged and is inverted from the FAA (see Figure S2 in the supporting information), there is ambiguity in the contributions of the bedrock topography and the density deficit of the sedimentary basin toward the total gravity anomaly, such that the basin thickness in these areas cannot be reliably recovered using gravity modeling alone.

3.2.2. Gravity Power Spectra Regression

Gravity power spectra provide a means of estimating the depth to major near-surface and intracrustal density discontinuities, such as the boundaries between ice and sediments, sediments and crystalline basement, and around midcrustal bodies and at the Moho (Damiani et al., 2014; Frederick et al., 2016). For a discrete number of density boundaries, the power spectra of the FAA will show an equal number of linear sections, each reflecting a different crustal density boundary. If the natural logarithm of power is plotted against the wave number, k (= 1/wavelength), the gradient of the resulting straight line is given by (Fairhead & Okereke, 1988; Karner & Watts, 1983)

$$\Delta \ln[\text{power}] = -4\pi d\, \Delta k \tag{1}$$

$$\frac{\Delta \ln[\text{power}]}{\Delta k} = s = -4\pi d \tag{2}$$

$$d = -\frac{s}{4\pi} \tag{3}$$

where d is the mean separation between the gravity continuation altitude (3,400 m) and the density boundary whose power spectrum slope is given by s. With the minimum resolvable wavelength of the FAA of ~9 km, the lower resolution limit of the power spectra is $k = 1/9 = 0.1111$ km^{-1}.

To determine sediment thickness using gravity power spectra, a 200 × 200 km moving window (Damiani et al., 2014; Frederick et al., 2016) was passed over the PPB. For each of twenty evenly spaced (but overlapping) windows, the gravity data were mirrored along both grid axes to produce 600 × 600 km grids to more accurately recover long-wavelength signals associated with deep intracrustal interfaces. The drawback of using a large window size is that the results represent average values for large areas. The results are, however, suitable as a means of independently constraining the results of the 2-D forward gravity models (section 3.2.1) and magnetic models (section 3.2.3) and identifying broad patterns in sediment thickness variation across the basin. A radial power spectrum was computed for each 200 × 200 km window in our newly assembled FAA grid using a fast Fourier Transform (Wessel et al., 2013). The power spectrum was plotted as the natural logarithm of power against radial wavenumber. We fitted a straight line to each linear segment of the spectrum using least squares regression (section 4.2). The gradient of each straight line was computed and used to estimate the depth to the corresponding crustal density interface (equation (3)).

3.2.3. Magnetic Depth-to-Source Modeling

Sediment thickness can also be independently estimated from magnetic data. Within a sedimentary basin, the depth to the source of magnetic anomalies is commonly interpreted as an estimate of the depth to the magnetic basement that underlies the nonmagnetic sedimentary succession (Frederick et al., 2016; Karner et al., 2005; Shepherd et al., 2006; Studinger et al., 2006, 2004). We derived depths to the magnetic sources beneath the PPB using multiple passes of Werner deconvolution along PolarGAP magnetic profile data (Ku & Sharp, 1983). In Werner deconvolution, a moving window is passed along the magnetic anomaly line data. The magnetic anomaly is detrended by removing the linear trend within the moving window. Detrended anomalies smaller than 5 nT are removed to eliminate solutions arising from noise in the data set. An upper limit (5 km) is placed on the permitted horizontal distance between the center of the moving window and the solution. Solutions outside this limit are commonly spurious and so are removed.

To determine depths from magnetic anomalies of a range of wavelengths, the size of the moving window can be incrementally increased and repeatedly passed along the profile. We used moving windows with widths of between 10 and 100 km, which correspond to the wavelengths of the highest and lowest frequency anomalies observed along the profiles. In each case, the window was shifted along the line in increments of 2.5 km. Solutions were sought at depths between the ice bed interface and a depth of 20 km to encapsulate the structure of the upper crust. The depth-to-source solutions were compared to the depth of the base of the sedimentary succession determined using 2-D gravity modeling.

3.3. Magnetic Anomalies

The relationship between subglacial topography and corresponding magnetic anomalies can be used to inform regional interpretations of subglacial geology in regions of Antarctica that lack surface rock exposures (Aitken et al., 2014; Ferraccioli et al., 2009; Studinger et al., 2004). We therefore examined the relationship between bedrock topography and magnetic anomalies along flight tracks over surface rock exposure, where the bedrock geology is known, and over ice-covered areas, where the geology must be inferred.

For visualization, we regridded the recent Antarctic magnetic anomaly compilation (ADMAP2.0; Golynsky et al., 2018) together with the PolarGAP magnetic anomaly data at 2.5 km horizontal resolution using a continuous curvature spline with a tension factor of 0.3 (Wessel et al., 2013; Figure 5d). The standard deviation of PolarGAP crossover errors was 47 nT, with the largest errors associated with long wavelength discrepancies on flights far from magnetic base stations during periods of extreme solar activity. Along-track errors are likely to be significantly lower in magnitude. We high-pass filtered the magnetic anomaly line data with a cutoff wavelength of 20 km and also computed the horizontal derivative of the magnetic anomaly; these products were used to aid our geological interpretations. Where high-frequency magnetic anomalies were correlated with subglacial topography, we employed a simple 2-D object-oriented magnetic model (Studinger et al., 2004) to determine the depth, geometry and likely lithology of the causative body.

4. Results

4.1. Bedrock Topographic Features and Associated Gravity Anomalies

New PolarGAP RES data reveal that the PPB is a 700 × 250 km elongated topographic depression, spanning an area of ~150,000 km^2 (Figures 3 and 4b). Present-day bedrock elevations within the basin range from

−2,160 m to +310 m (relative to modern-day sea level), with an average elevation of −490 m. A major system of deep subglacial valleys forms a left-stepping en echelon pattern along the eastern margin of the basin (Figure 4b). The valley floors are observed at depths of at least 1.5 km below sea level, although they are often not imaged by RES (Figure 6). The average ice thickness in the basin is 2.84 km, and the ice thickness commonly exceeds 3 km across inland parts of the basin (Figure S3). The total volume of ice within the basin is 3.9×10^5 km^3, of which 3.1×10^5 km^3 lies above present-day sea level. The sea level equivalent of this volume is ~80 cm.

Gravity anomalies show that the PPB is characterized by a broad low FAA, which largely reflects the subglacial topography (Figures 5a and 6a). The presence of deep troughs within the basin is confirmed by FAA lows of up to −100 mGal (Figure 5a). These troughs raise no signal in the Bouguer and isostatic anomalies in locations where the FAA was inverted for bedrock elevation under the assumption of a purely topographic source (section 3.1); "backfilling" these troughs with rock-equivalent densities for the Bouguer correction removes most of the signal beyond that arising from the difference between the correction density and the true density of the rocks the troughs intersect. The PPB as a whole is characterized by a broad Bouguer anomaly low. The Bouguer and isostatic anomalies both show steady increases along the basin's long axis (Figures 5b and 5c).

When the bedrock elevations are isostatically rebounded for the removal of the modern ice load, the southern (upstream) region of the basin is situated on average at +500 m elevation, whereas the northern end of the basin lies close to or just below sea level (Figure 4b). Hereafter, we refer to the "southern" and "northern" PPB, which we define as being separated by the profile X–X′ (shown in Figure 4b), approximately coincident with the sea level contour in the rebounded bedrock topography (Figure 4b). Across the higher-elevation southern PPB, we mapped a series of steep-sided, flat-topped topographic "highs" that resemble mesas or buttes. These features typically extend over length scales of <20 km, with elevations of up to 500 m and steep flanks commonly >60° and often correspond to high-frequency magnetic anomalies (see section 4.3). In the northern PPB, this mesa-like topography is not observed; the ice sheet bed is instead characterized by a smooth-topped topographic block approximately 60 km across that tilts downward toward the east at an angle of ~0.5°, and which is bounded on both sides by deep subglacial troughs (see section 4.3).

4.2. Sedimentary Basin Thickness

Our forward gravity models indicate that the PPB hosts a significant thickness of sedimentary rocks (Figures 7 and 8). The average thickness of sedimentary rocks is 1.6 km, and the maximum thickness is 3.7 km. The forward modeled sediment thickness estimates are associated with a margin of error due to individual uncertainties in the assumed sediment density and effective elastic thickness. We find that the associated uncertainties in the modeled sediment thickness are ±700 m (Figure 7). However, this is a systematic uncertainty, which applies to the magnitude of sediment thickness rather than the pattern.

The isopachs define an elongate-bowl shape, with the greatest thicknesses located in the central and southern PPB (Figure 8a). We note, however, that these maxima occur in a region of relatively sparse coverage in RES and gravity data (Figures 3 and 4). Our modeling indicates that the subglacial topography alone is approximately sufficient to account for the observed gravity over the northern PPB; the gravity data indicate sediment thicknesses of <1 km, which is close to the resolvable limit due to the uncertainties inherent in the modeling process (Figure S4). Moreover, the observation that the southern PPB is situated ~500 m higher than the northern PPB (Figure 3), but associated with an equally low free-air gravity anomaly (Figure 5a), implies the presence of lower density rocks across the southern PPB, as does the decrease in the isostatic anomaly over the southern PPB (Figure 5c).

Linear regression of the FAA power spectra reveals three distinct density boundaries (e.g., Figure 8b). The depth of the boundaries varies spatially, with ranges of 2.8–4.4 km (boundary 1), 5.6–8.7 km (boundary 2), and 12–15 km (boundary 3) below the gravity continuation datum. The depths to the three density interfaces were converted to elevations relative to sea level by subtracting the depths from the continuation altitude (3,400 m). The first (shallowest) interface is interpretable as the base of the ice sheet. Its elevation is comparable to that of the radar-derived bedrock surface (Figure 3 and Table S1 in the supporting information). The second interface resides at depths of 2.2–5.3 km below sea level and is interpretable as the base of the sedimentary basin because it broadly corresponds to that feature as determined by forward gravity modeling and

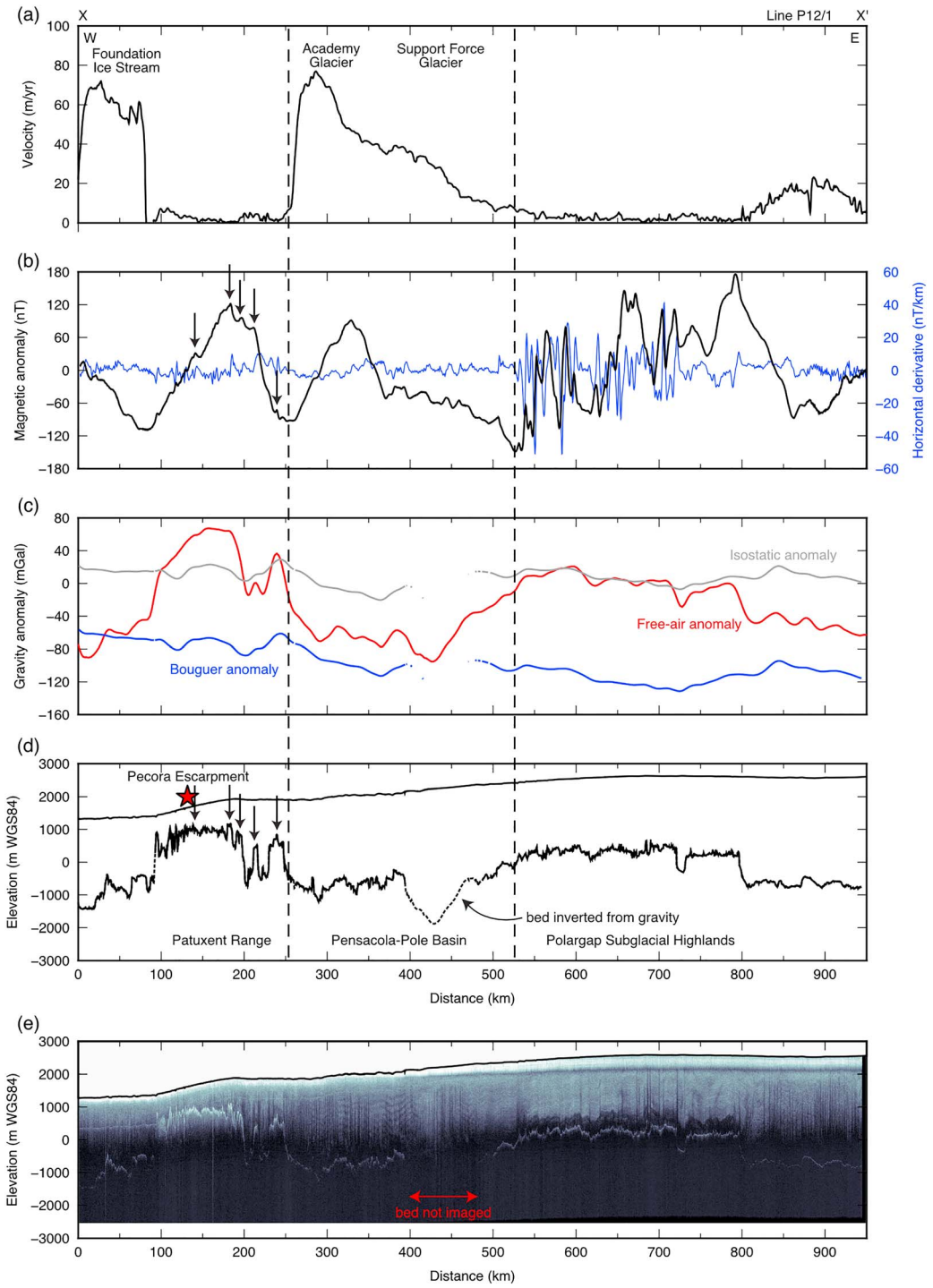

Figure 6. Subglacial topography, gravity anomalies, magnetic anomalies, and surface velocity across the Pensacola-Pole Basin (PPB; line P12/1; profile X-X′ in Figure 4). (a) Ice surface velocity (Rignot et al., 2011). (b) Magnetic anomaly (black) and its horizontal derivative (blue). The magnetic anomaly changes abruptly across the eastern edge of the PPB, dividing the Polargap Subglacial Highlands, which exhibit high amplitude (~100 nT), high-frequency anomalies, from the Pensacola-Pole Basin and Patuxent Range, which show much lower amplitude (<20 nT) high-frequency anomalies. (c) Free-air (red), Bouguer (blue), and flexural isostatic (gray) gravity anomalies. (d) Elevation of the ice surface and bed. Solid lines indicate picks observed in the radargram (panel e); dashed lines indicate areas where the bed is not visible in the RES data and the elevation is inferred from the free-air gravity anomaly (assuming no change in bedrock density along the profile). Arrowed lines (also shown in panel b) indicate flat-topped bedrock surfaces in the Patuxent Range, which coincide with high-frequency (~10 km wavelength) magnetic anomaly highs. The red star marks the location of the Pecora Escarpment, where Jurassic Ferrar dolerites crop out at the surface. Vertical dashed lines demarcate the eastern and western boundaries of the PPB. (e) Radar echogram. Elevations are given relative to the WGS84 ellipsoid.

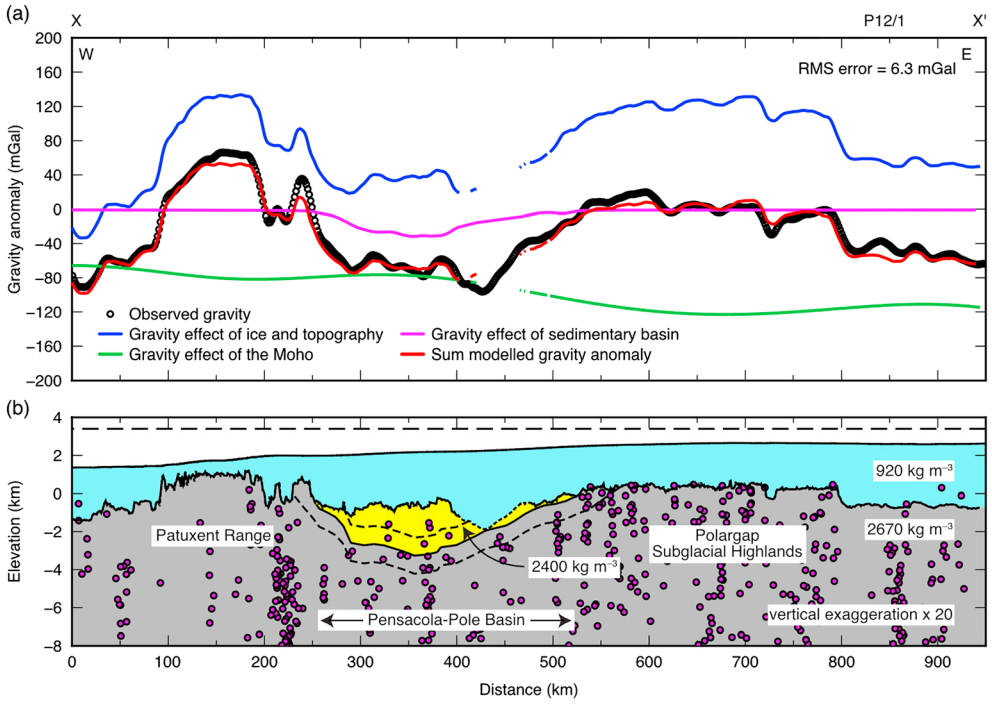

Figure 7. Gravity model along profile X–X′ (line P12/1). (a) Observed and calculated gravity anomalies, including modeled gravity effects of the ice and bedrock topography, the Moho, and the sedimentary basin. A long-wavelength (>1,200 km) signal has been removed from the gravity field. All gravity effects were computed at 3,400 m, corresponding to the maximum flight altitude/upward continuation datum for the gravity surveys (marked by the black dashed line in panel b). The root-mean-square error between the observed and modeled gravity anomaly is 6.3 mGal. (b) Results of the model, showing the thickness of sedimentary rocks required to match the observed gravity "low" over the basin. The dashed lines show the range of uncertainty of the depth of the basin based on expected variability in sediment density and effective elastic thickness. Magenta circles are estimates of the depth to magnetic source. Note that there is uncertainty in the modeled sediment thickness where the bed is not imaged by the radar data, and consequently, the relative gravity effects of the topography and the sedimentary basin are ambiguous.

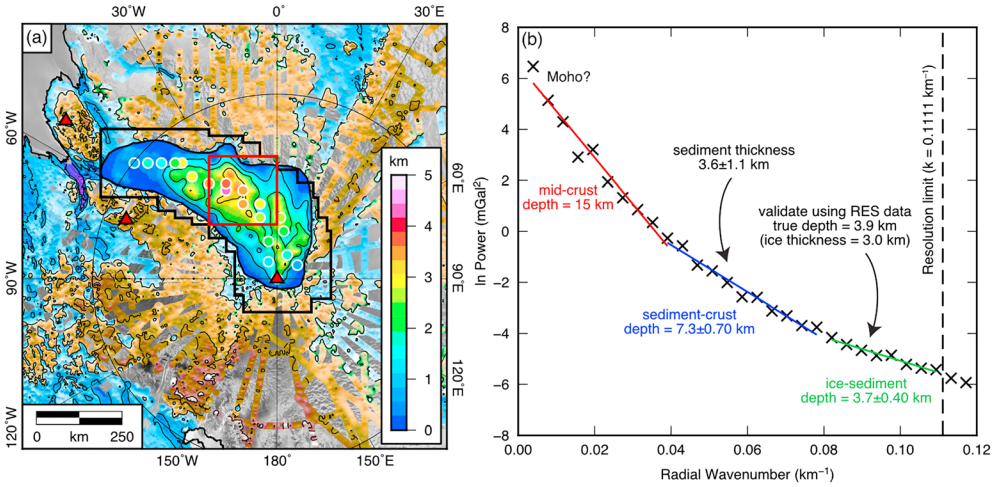

Figure 8. Thickness of the sedimentary rocks within the Pensacola-Pole Basin. (a) Isopach map produced by gridding sediment thicknesses determined using 2-D forward gravity models (Figure 7). Contour interval is 1 km. Colored circles denote the sediment thickness determined within a 200 × 200 km moving window using the spectral method (panel b). Circles are located at the center of each window. Red filled triangles show the locations of seismic stations. The background shows the present-day bedrock elevation, using the same color scale as in Figure 3. (b) Sediment thickness determination using power spectra (corresponding to red box in panel a). The observed gravity spectrum within each window (moving window outlines are shown by black lines in panel a) comprises three linear sections separated by breaks of slope. The gradient of these sections reveals the depth to the corresponding crustal interface (below the gravity continuation altitude of 3,400 m).

magnetic depth-to-source estimation. The third interface likely represents a midcrustal boundary (e.g., the base of the upper crust). The window size was likely insufficient to capture the long-wavelength signals associated with deeper crustal interfaces or the Moho.

With these interpretations, the height between boundaries 1 and 2 is interpretable as the average thickness of sedimentary rocks within the moving window. This spectrally derived sediment thickness varies from 0.70 ± 0.90 to 4.3 ± 1.1 km across the basin (Figure 8a and Table S1). We emphasize the significant qualitative uncertainty in these estimates, which is related to a number of factors: (i) breaks of slope in the power spectra are identified by eye (and are often relatively gradational; Figure 8b), (ii) scatter in the power spectra, (iii) the uneven distribution of survey lines across the basin (Figure 1a), and (iv) the spectral contents of some of the windows are likely to be influenced by geology outside the sedimentary basin (Figure 8a).

Despite this, there are a number of reasons why we expect the spectral results to be generally reasonable. First, in 19 of the 20 windows, the power spectrum recovered the elevation of the ice bed interface to within ±500 m of the average RES-derived elevation (Table S1), indicating that the spectrum can reliably recover the depth of this interface. Second, the spectrally derived sediment thickness falls between the average and the maximum sediment thickness determined from forward gravity modeling in sixteen of the windows (Table S1). Finally, the results of both gravimetric approaches exhibit a consistent pattern whereby thicknesses are largest in the central and southern PPB and decrease toward the northern end of the basin (Figure 8a).

We also compared the gravimetric sedimentary basin base to the depth of magnetic sources isolated using Werner deconvolution. In an idealized sedimentary basin, all of whose basement rock is sufficiently magnetic to be detected as a source of observed anomalies, magnetic sources represent the base of the sedimentary succession. In reality, however, the basement may comprise weakly or nonmagnetic metasedimentary rocks, which do not have a strong magnetic signature, and intrusive igneous rocks within the basin fill may give shallow depth-to-source solutions. We find that magnetic sources cluster at the ice sheet bed over the highlands to the east of the PPB, indicating that basement rocks are "exposed" at the bedrock surface. Moving westward over the PPB, the source depth tends to increase, and significant clustering of magnetic sources is observed within 1 km of the modeled base of the sedimentary basin (Figure 7). Although significant scatter is evident in the solutions, the overall pattern of the depth-to-source estimates lends broad independent support to our modeled basin geometry.

4.3. Magnetic Anomaly Features

Over the basement complex exposed in the southern TAM, the magnetic field exhibits a series of high-amplitude (up to 300 nT), short-wavelength (up to 30 km) magnetic highs and lows (Figure 9a). Across the Thiel and Pensacola Mountains, basement rocks are associated with magnetic anomaly highs with (peak-to-trough) amplitudes of up to 150 nT (Figure 9b). The Ferrar dolerites exposed at Lewis Nunatak and the Pecora Escarpment are associated with high-frequency magnetic anomaly highs of 10–50 nT with wavelengths of ~10 km (Figure 9b).

Moving inland over ice-covered East Antarctica, the amplitudes of the magnetic anomalies are generally lower than those observed above rock exposures. Within the southern PPB, the magnetic field comprises a series of high-frequency anomaly couplets with amplitudes of 10–30 nT (Figure 9d). These high-frequency anomalies commonly coincide with mesas observed in the subglacial topography (Figure 9d). Two-dimensional object-oriented magnetic modeling indicates that these anomalies can be explained by the presence of thin magnetic sills situated close to the ice sheet bed (Figure 10). Consistent with this, depth-to-source solutions derived from Werner deconvolution (Figure 10) indicate that the causative bodies associated with these magnetic anomalies are situated at shallow depths (within 1 km of the ice sheet bed). In the northern PPB, the association of high-frequency magnetic anomalies with topographic mesas is not widely observed. Instead, the observed magnetic anomaly within the northern PPB exhibits long wavelengths (80–100 km) and up to 300 nT peak-to-trough amplitudes (Figure 9c).

We mapped the association of high-frequency magnetic anomalies and topographic mesas across the study region and assigned a "confidence factor" from 1 to 3, reflecting the likelihood that each mapped feature reflected a magnetic sill (Figure 11). A factor of 3 indicates a magnetic high whose location corresponds closely to a clear topographic mesa; a factor of 2 indicates a high-frequency magnetic high which is not clearly

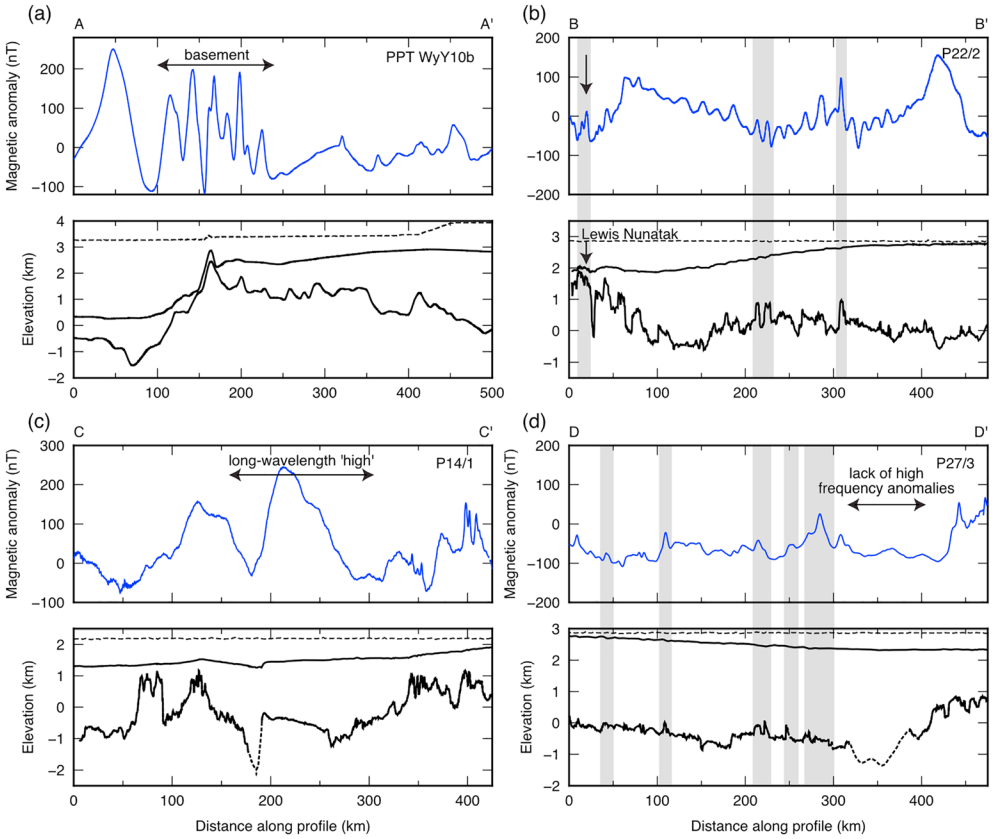

Figure 9. Magnetic anomalies in the Pensacola-Pole Basin (PPB) and surrounding highlands. (a) Profile A–A′ (Pensacola-Pole Transect line WyY10b, Studinger et al., 2006) across the southern Transantarctic Mountains. Upper panel shows the magnetic anomaly (blue line); lower panel shows the ice sheet surface and bed (solid lines) and the flight altitude (dashed line). The exposed Neoproterozoic-Cambrian basement rocks of the southern TAM (100–240 km along the profile) are characterized by high-amplitude, short-wavelength (<30 km) magnetic anomalies superimposed on a broad high. (b) Profile B-B′ (PolarGAP line P22/2) from the Thiel Mountains to South Pole. A high-frequency (10–20 km) magnetic anomaly high of ~50 nT is observed over the Lewis Nunatak, where Ferrar dolerites crop out. Similar high-frequency anomalies corresponding to mesa-like subglacial topography are indicated by the shaded regions. (c) Profile C-C′ (PolarGAP line P14/1) crossing the northern PPB. The magnetic anomaly over the basin (160–300 km along the profile) is dominated by a long-wavelength "high" of up to 250 nT. High-frequency anomalies are absent over the basin. (d) Profile D-D′ (PolarGAP line P27/3) crossing the southern PPB. Shaded regions indicate correlated ~50 nT high-frequency (<20 km) magnetic anomalies and topographic mesas. The bed is not imaged along the northeastern margin of the basin (320–400 km along the profile), where the FAA is indicative of deep subglacial topography. This section of the line is notable for the absence of high-frequency magnetic anomalies. All profile locations are shown in Figure 5d.

correlated to a subglacial topographic feature; and a factor of 1 indicates a mesa that is not associated with a clear magnetic anomaly. The eastern margin of the basin is demarcated by an abrupt change in the signature of the magnetic anomaly between the PPB and the Polargap Subglacial Highlands (Figure 6b). The Polargap Subglacial Highlands exhibit high-amplitude (up to ~150 nT), high-frequency magnetic anomalies and large horizontal magnetic gradients (Figure 6b).

5. Discussion

5.1. Geology of the Pensacola-Pole Basin

Our gravity and magnetic analyses indicate that the PPB contains a succession of sedimentary rocks 2–3 km in thickness (Figures 7 and 8). Modeled sediment thicknesses show a decrease from as much as 3.7 km in the southern PPB to ~1 km in the northern PPB and 1–2 km close to South Pole. Independent seismic reflection and refraction constraints on sediment thickness in East Antarctica are sparse. However, a seismic refraction survey (Bentley, 1991) and electrical resistivity data from a magnetotelluric survey (Wannamaker et al., 2004) carried out close to the South Pole indicate the presence of a 1–2 km thick layer of sedimentary rocks. These values are in good agreement with our gravimetric sediment thicknesses in this vicinity (Figure 8). Additionally, Studinger et al. (2006) suggest that the subdued expression of a magnetic lineament close to

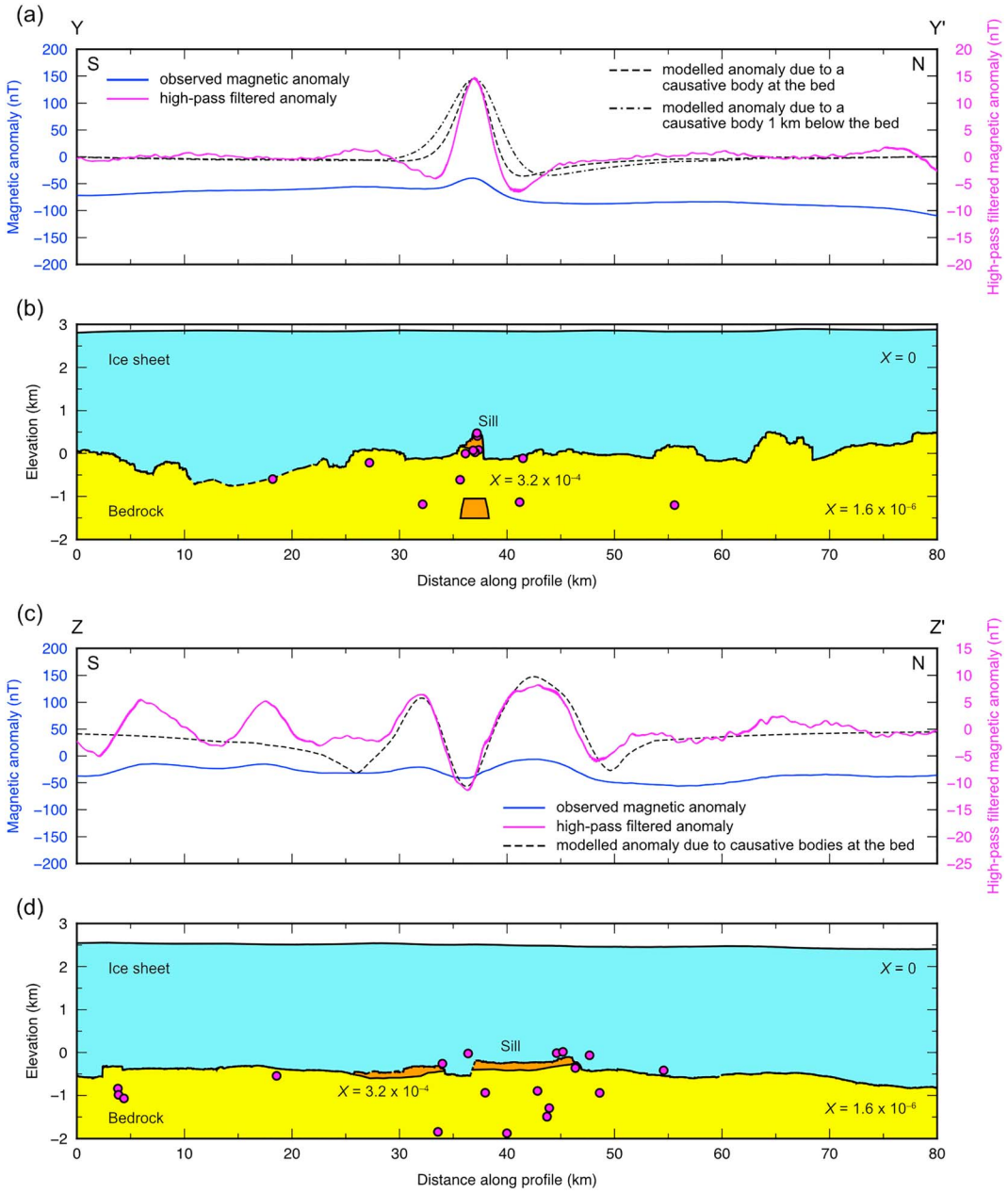

Figure 10. High-frequency magnetic anomalies and mesa topography in the Pensacola-Pole Basin. (a and c) Observed and modeled magnetic anomaly along profiles Y–Y′ and Z–Z′. The blue line shows the magnetic anomaly, and the magenta line shows the anomaly after high-pass filtering. (b and d) Magnetic models in which the observed magnetic anomaly highs of 10–20 nT over topographic mesas are explained the presence of magnetic sills at the ice sheet bed (orange polygons). For comparison we model the effect of a magnetic body at 1 km below the bed along Y–Y′ (in panel b). Magenta circles show the location of Werner deconvolution "depth-to-source" solutions. Placing the causative bodies at the bed yields a close match with the observed wavelength of the magnetic anomaly high. Depth-to-source solutions also show clustering near the bed. This suggests that the mesas arise due to the presence of shallow magnetic bodies of erosion-resistant igneous rocks, as in the commonly-observed association of Ferrar dolerites intruded into Beacon Supergroup sedimentary rocks. Apparent magnetic susceptibilities (X) are in SI units and are typical values for ice, weakly or nonmagnetic bedrock (e.g. Beacon Supergroup sedimentary rocks), and Ferrar dolerites (Studinger et al., 2004). Profile locations are shown in Figure 11.

the South Pole may be attributed to an infill of nonmagnetic sedimentary rocks. Some authors (Bentley, 1991; Wannamaker et al., 2004) conjecture that this sediment is an inland extension of the Beacon Supergroup, which is exposed in the southern TAM and Victoria Land. However, the age and stratigraphy of the sedimentary succession within the PPB remain unknown.

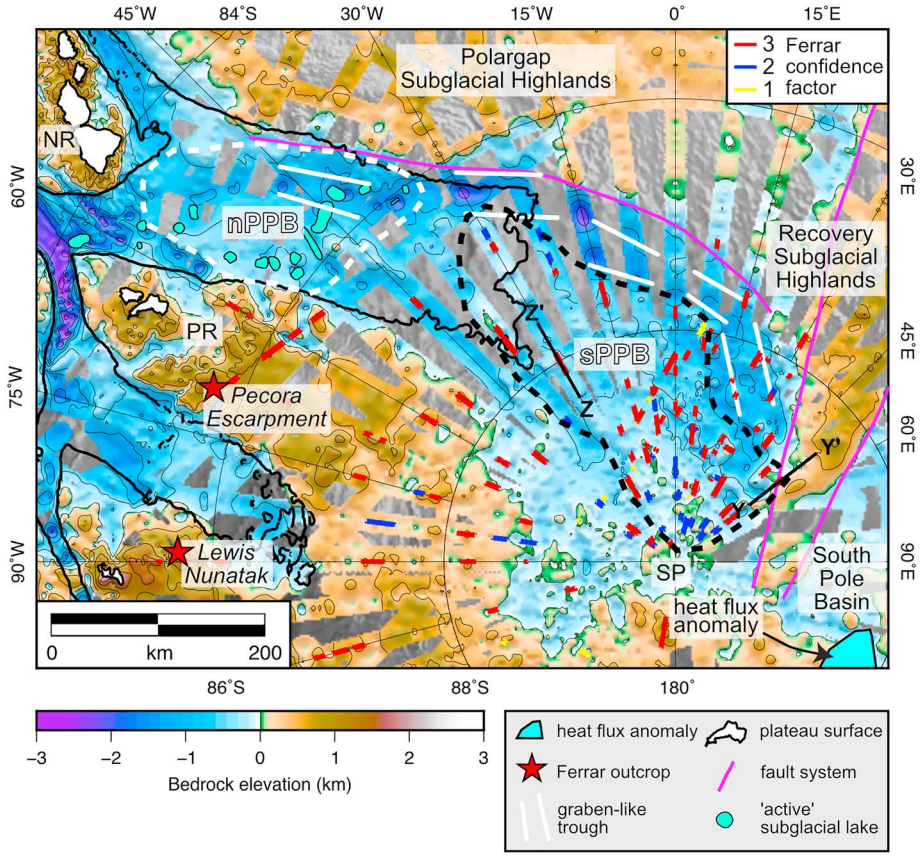

Figure 11. Geology of the Pensacola-Pole Basin (PPB) overlain on the present-day subglacial topography. Colored lines show the location of high-frequency magnetic anomalies and mesa topography as observed along flight lines. Lines are colored according to the 'confidence factor' (from high to low confidence: red = 3; blue = 2; yellow = 1; see text for details). Abbreviations: NR = Neptune Range; PR = Patuxent Range; SSouth Pole. White and black dashed outlines show the northern (nPPB) and southern PPB (sPPB), which are distinguished by their subglacial topography, sediment thickness, and presence/absence of Ferrar-like magnetic anomalies. Black solid line marks the 20 m/year ice surface velocity contour (Rignot et al., 2011). Subglacial and subaerial features of interest are labeled in the legend. Major subglacial fault systems (magenta lines; Ferraccioli et al., 2011; Jordan et al., 2018; Lough et al., 2018), the geothermal heat flux anomaly near South Pole (blue polygon; Jordan et al., 2018), and "active" subglacial lakes (turquoise; Smith et al., 2009) have been previously documented. The locations of profiles Y–Y′ and Z–Z′ and (shown in Figure 10) are indicated.

Apatite fission track (AFT) and (U-Th)/He thermochronology data, alongside thermal history modeling, have been interpreted as reflecting two phases of burial of the basement along the East Antarctic margin from Victoria Land to Coats Land by sedimentary successions since the mid-Paleozoic (Krohne et al., 2016; Lisker et al., 2014; Lisker & Läufer, 2013; Prenzel et al., 2018). The first phase was associated with the deposition of Beacon Supergroup strata along the subduction-dominated Panthalassan margin of Gondwana in a series of basins referred to collectively as the Transantarctic Basin (Collinson et al., 1994). The second commenced in the Jurassic following emplacement of the Ferrar Large Igneous Province, the onset of rifting in the Weddell Sea, and the subsequent breakup of Gondwana and onset of seafloor spreading between Africa and East Antarctica (Jordan et al., 2017; Leinweber & Jokat, 2012). AFT data indicate that up to 4 km of post-Jurassic sediments were deposited in a "Mesozoic Victoria Basin" that extended from Coats Land to Victoria Land (Krohne et al., 2016; Lisker et al., 2014; Lisker & Läufer, 2013; Prenzel et al., 2018), although such rocks have not been directly observed in East Antarctica.

The strong correlation of mesa-like topography with high-frequency magnetic anomalies observed within the southern PPB (Figure 9–11) resembles those generated by sills of Jurassic Ferrar dolerite capping siliciclastic Beacon Supergroup strata, as observed in the Theron Mountains, western Dronning Maud Land, central Transantarctic Mountains, Victoria Land, and Wilkes Subglacial Basin (Chiappini et al., 2002; Ferraccioli et al., 2009, 2005; Ferraccioli & Bozzo, 2003, 1999; Forsberg et al., 2018; Goodge & Finn, 2010;

Shepherd et al., 2006; Studinger et al., 2004). Moreover, the amplitudes (10–30 nT) and wavelengths (<20 km) of the magnetic anomalies across the southern PPB are consistent with those observed where Ferrar dolerites crop out in the study area—at the Pecora Escarpment and Lewis Nunatak (Figure 11). This indicates that Beacon and Ferrar rocks may also be preserved within the southern PPB, where they may constitute a significant fraction of the total sediment thickness.

Magnetic anomaly modeling and depth-to-source estimates (Figure 10) indicate that magnetic bodies consistent with Ferrar dolerite sills are situated close to (within 1 km of) the bed across the southern PPB. The presence of mesa-like topography there also indicates that Beacon/Ferrar rocks lie at depths sufficiently shallow to exert an influence on the geomorphology of the ice sheet bed. This precludes the presence of significant thickness of post-Jurassic sediments in the southern PPB, suggesting that any post-Jurassic sediment is relatively thin and spatially limited.

Since the PPB is situated between two known major Beacon Supergroup depocentres in Victoria Land and Coats Land (Barrett, 1991; Collinson et al., 1994), it is realistic to expect that Beacon sedimentary rocks were also deposited in this region. Offshore sediment εNd values (the deviation of the measured $^{143}Nd/^{144}Nd$ ratio from the chondritic value of 0.512638 in parts per 10,000) in the southeastern Weddell Sea range between −7 and −10 (Roy et al., 2007; Walter et al., 2000). These values are consistent with the mixing of onshore source material from Beacon Supergroup rocks, the Lower Paleozoic rocks from which the Beacon is derived (Goodge & Finn, 2010), and Ferrar dolerites (Cook et al., 2013). Moreover, heavy mineral assemblages in glaciogenic sediments in the Weddell Sea are consistent with derivation from Beacon sediments and mafic igneous rocks (e.g., Ferrar dolerites and Dufek gabbros; Diekmann & Kuhn, 1999), which are also exposed in the Theron Mountains and Whichaway Nunataks (Brook, 1972).

Magnetic anomalies and subglacial topography in the northern PPB do not resemble those of the Beacon/Ferrar (Figure 11). Moreover, airborne gravity data do not resolve a significant (>1 km) thickness of sediment in this region (Figure 8). The en echelon system of subglacial troughs along the eastern margin of the PPB also lacks high-frequency magnetic anomalies (Figure 9d), suggesting that Beacon/Ferrar rocks are not preferentially preserved within these basins, although it is possible that magnetic sources are present at significant depth, such that high-frequency magnetic anomalies have been attenuated.

The Polargap Subglacial Highlands also exhibit high-frequency magnetic anomalies, but the amplitudes of these anomalies exceed those observed where Ferrar dolerites crop out in the survey area (Figure 5d). These anomalies are instead more consistent with those observed over basement rocks outcrops in this region. Gravity anomalies over the highlands (Figures 5a–5c) are similarly inconsistent with a significant cover of lower-density Beacon Supergroup rocks. The Recovery Subglacial Highlands truncate the PPB close to South Pole (Figure 3). High-frequency magnetic anomalies appear to be absent from the South Pole Basin (north of the South Pole along 90°–120°E; Figures 3 and 11), although we note that this region is only sampled by six PolarGAP flight lines (Figure 1). The basin may instead be underlain by Proterozoic basement and granitoids (Jordan et al., 2018). This change in geology and the step change in the frequency content of the magnetic anomaly across the eastern margin of the PPB (Figure 6b) are consistent with the hypothesis that the Polargap and Recovery Subglacial Highlands are bounded by a major geological boundary or fault system (Ferraccioli et al., 2011; Jordan et al., 2018), demarcating the PPB from the East Antarctic interior (Figure 11). Earthquake focal mechanisms indicate that range-flanking faults remain active at the present-day (Lough et al., 2018).

Although difficult to resolve with the available geophysical data, the asymmetric geometry of the PPB resembles that of half-graben basins in the East African Rift System (Ebinger et al., 1991). The asymmetry of the PPB suggests that its eastern margin is fault bounded, and its western margin is defined by flexure and tilting of the fault's hanging-wall block (Figure 11). We suggest that in the future, increased coverage of geophysical data and more sophisticated 2-D or 3-D geophysical modeling (e.g., simultaneous inversions of gravity and magnetic anomalies) along key profiles could lead to improved understanding of the tectonic and geological evolution of the PPB.

5.2. Influence of Topography and Geology on Ice Sheet Dynamics

If the sedimentary succession within the PPB is predominantly coeval with the Beacon Supergroup, the basin is a long-lived tectonic and topographic feature. We suggest that this means the basin is likely to

have influenced the behavior of this sector of the EAIS since its inception. Notably, the subglacial troughs along the eastern margin of the PPB do not clearly correlate with the modern-day ice surface velocity field (Figures 1b and 6a and 6d), implying they are not currently being actively incised beneath the modern EAIS. There is also no clear relationship between the locations of these troughs and of active subglacial lakes (Figure 11) mapped from repeat-pass satellite altimetry (Smith et al., 2009). Each of the mapped lakes is located in the northern PPB (although it should be noted that satellite tracks do not cover the area south of 86°S). Together these observations suggest that if the troughs are erosional features, then they were likely selectively eroded beneath an earlier, more restricted, ice sheet that was steered along the pre-existing geological structure of the eastern margin of the basin, as has been suggested for a range of tectonically controlled subglacial troughs/grabens across Antarctica (Bingham et al., 2012; Ferraccioli et al., 2011; Jordan et al., 2013; Paxman et al., 2017; Figure 11).

Figures 3 and 4 show that once formed, these deep troughs would have been situated below sea level regardless of the extent of ice overlying them. The implication of this is that during a period of ice sheet retreat and marine incursion, the possibility would arise for the deposition of marine sediments in the areas situated below sea level, which extend to 800 km inland of the modern grounding line. Although geophysical data rule out any significant thickness of such sediments within the PPB, they do not preclude the presence of a relatively thin, unresolvable (<1 km) drape of marine sediment. In West Antarctica, the distribution of deformable subglacial sediments is thought to influence the onset zones and lateral margins of ice streams (Bell et al., 1998; Ross et al., 2012; Studinger et al., 2001). In the PPB, however, there is little evidence for enhanced flow or onset of streaming focused above areas of the bed that are situated below sea level after rebounding for ice unloading (Figures 1b and 4b). This suggests that these regions do not contain deformable marine sediment that is capable of modulating ice flow. Thermodynamic modeling and analysis of internal layers within the EAIS indicate that under full glacial conditions during the Last Glacial Maximum, ice streaming may have occurred as far inland as South Pole (Beem et al., 2018), which may have caused erosion of deformable sediment.

Aside from the distribution of deformable subglacial sediment, a number of other mechanisms are hypothesized to control the onset of ice streams, including topographic focusing (Diez et al., 2018), topographic steps, topographic roughness (Bingham & Siegert, 2009; Rippin et al., 2014), geothermal heat flux, subglacial geology, and subglacial meltwater distribution and routing (Langley et al., 2014; Winsborrow et al., 2010). Indeed, drawdown of englacial layers ~150 km grid southeast of South Pole (Figure 1) indicates the presence of a region of enhanced basal melting due to anomalously high geothermal heat flux, which likely exerts an influence on regional subglacial hydrology and ice sheet dynamics (Jordan et al., 2018).

It is therefore noteworthy that subglacial geomorphology and the gravity and magnetic anomalies presented in this study indicate that Beacon and Ferrar rocks are preserved in the southern PPB, where ice is slow moving, but are largely absent in the northern PPB, where ice is fast flowing. The onset of streaming approximately coincides with the transition in subglacial geology from the southern PPB to the northern PPB (Figure 11). We note two possible hypotheses that could explain this observation. One possibility is that enhanced flow in the northern PPB has eroded much of the Beacon/Ferrar material and thus that the change in geology is a result of the ice velocity field. Alternatively, it is possible that no Beacon Supergroup rocks were ever deposited in the northern PPB due to a lack of accommodation space and thus that a preexisting change in subglacial geology influences the location of ice streaming onset. We highlight that these hypotheses are testable with further geophysical data acquisition and analyses, and the tests may yield significant insight into the potential subglacial controls on the dynamics of this sector of the EAIS.

6. Conclusions

Based on our analysis, we make the following conclusions:

1. Our new bedrock topography compilation reveals that the PPB is situated on average 490 m below sea level, with a system of overdeepened troughs trending along the eastern margin of the basin (~1.5 km below sea level). These troughs follow a major geological boundary and extend to 800 km inland of the grounding line. However, overlying ice velocities are not strongly elevated, indicating that these troughs were likely eroded beneath an earlier EAIS, with a grounding line situated inland of its present-day position.

2. Forward gravity modeling, spectral analysis, and magnetic depth-to-source estimates suggest that the PPB is underlain by a 2–3 km thick sedimentary succession. The geophysical characteristics of the PPB are consistent with the presence of Paleozoic Beacon Supergroup and intermittently preserved Jurassic Ferrar dolerites across the southern part of the basin. The northern part of the PPB does not contain a significant thickness of sedimentary cover, although airborne gravity data do not preclude the presence of a thin (<1 km) drape of (marine) sediment on top of underlying basement rocks.
3. Our findings indicate that the PPB is a long-lived geological and topographic feature that may have exerted an influence on the behavior of the EAIS throughout the Oligocene–Neogene. Although there is no clear correspondence between ice sheet velocity and subglacial topography and geology based on the data acquired, it may be possible in the future to test whether enhanced flow in the northern PPB has eroded much of the Beacon/Ferrar material, or instead whether a preexisting change in subglacial geology influences the onset of ice streaming.

Acknowledgments
G. J. G. P. is in receipt of a Natural Environment Research Council UK studentship NE/L002590/1, and S. S. R. J. is supported by NERC grant NE/R000824/1. Financial support for the PolarGAP project was provided by the European Space Agency. The authors wish to extend especial thanks to the PolarGAP field team for the collection of the airborne geophysical data. We thank the British Antarctic Survey and the Center for Ice, Climate and Ecosystems (ICE) of the Norwegian Polar Institute for field and logistics support and Danish Technical University (DTU) staff for their contributions in data collection and laser altimetry processing. We also thank the National Science Foundation (NSF) for providing access to and field support at South Pole station. We are also grateful to Angelika Humbert and the Alfred Wegener Institute (AWI) Glaciology section for providing access to the RECISL radar and gravity data sets. We thank John Goodge, Carol Finn, and an anonymous reviewer for their constructive reviews, which greatly improved the quality of the manuscript. PolarGAP airborne geophysical data used in this article are available from the European Space Agency data portal (https://earth.esa.int/web/guest/campaigns). ICECAP and Operation IceBridge data products used in this study are available through the IceBridge data portal at the National Snow and Ice Data Center (http://nsdic.org/icebridge/portal/). Grids and figures were produced using the Generic Mapping Tools (GMT) software package (Wessel et al., 2013).

References

Aitken, A. R. A., Roberts, J. L., van Ommen, T. D., Young, D. A., Golledge, N. R., Greenbaum, J. S., et al. (2016). Repeated large-scale retreat and advance of Totten Glacier indicated by inland bed erosion. *Nature*, *533*, 385–389. https://doi.org/10.1038/nature17447

Aitken, A. R. A., Young, D. A., Ferraccioli, F., Betts, P. G., Greenbaum, J. S., Richter, T. G., et al. (2014). The subglacial geology of Wilkes Land, East Antarctica. *Geophysical Research Letters*, *41*, 2390–2400. https://doi.org/10.1002/2014GL059405

Anandakrishnan, S., Blankenship, D. D., Alley, R. B., & Stoffa, P. L. (1998). Influence of subglacial geology on the position of a West Antarctic ice stream from seismic observations. *Nature*, *394*, 62–65.

Bamber, J. L., Ferraccioli, F., Joughin, I., Shepherd, T., Rippin, D. M., Siegert, M. J., & Vaughan, D. G. (2006). East Antarctic ice stream tributary underlain by major sedimentary basin. *Geology*, *34*, 33–36. https://doi.org/10.1130/G22160.1

Barrett, P. J. (1991). The Devonian to Triassic Beacon Supergroup of the Transantarctic mountains and correlatives in other parts of Antarctica. In R. J. Tingey (Ed.), *The Geology of Antarctica*, (pp. 120–152). Oxford, UK: Oxford University Press.

Beem, L. H., Cavitte, M. G. P., Blankenship, D. D., Carter, S. P., Young, D. A., Muldoon, G. R., et al. (2018). Ice-flow reorganization within the East Antarctic Ice Sheet deep interior. *Geological Society, London, Special Publications*, *461*, 35–47. https://doi.org/10.1144/SP461.14

Bell, R. E., Blankenship, D. D., Finn, C. A., Morse, D. L., Scambos, T. A., Brozena, J. M., & Hodge, S. M. (1998). Influence of subglacial geology on the onset of a West Antarctic ice stream from aerogeophysical observations. *Nature*, *394*, 58–62. https://doi.org/10.1038/27883

Bell, R. E., Ferraccioli, F., Creyts, T. T., Braaten, D., Corr, H., Das, I., et al. (2011). Widespread persistent thickening of the East Antarctic ice sheet by freezing from the base. *Science*, *331*, 1592–1595. https://doi.org/10.1126/science.1200109

Bentley, C. R. (1991). Configuration and structure of the subglacial crust. In R. J. Tingey (Ed.), *The Geology of Antarctica*, (pp. 335–364). Oxford Science Publications.

Bingham, R. G., Ferraccioli, F., King, E. C., Larter, R. D., Pritchard, H. D., Smith, A. M., & Vaughan, D. G. (2012). Inland thinning of West Antarctic Ice Sheet steered along subglacial rifts. *Nature*, *487*, 468–471. https://doi.org/10.1038/nature11292

Bingham, R. G., Rippin, D. M., Karlsson, N. B., Corr, H. F. J., Ferraccioli, F., Jordan, T. A., et al. (2015). Ice-flow structure and ice dynamic changes in the Weddell Sea sector of West Antarctica from radar-imaged internal layering. *Journal of Geophysical Research: Earth Surface*, *120*, 655–670. https://doi.org/10.1002/2014JF003291

Bingham, R. G., & Siegert, M. J. (2009). Quantifying subglacial bed roughness in Antarctica: implications for ice-sheet dynamics and history. *Quaternary Science Reviews*, *28*, 223–236. https://doi.org/10.1016/j.quascirev.2008.10.014

Bingham, R. G., Siegert, M. J., Young, D. A., & Blankenship, D. D. (2007). Organized flow from the South Pole to the Filchner-Ronne ice shelf: An assessment of balance velocities in interior East Antarctica using radio echo sounding data. *Journal of Geophysical Research*, *112*, F03S26. https://doi.org/10.1029/2006JF000556

Blankenship, D.D., Kempf, S.D., Young, D.A., 2017. IceBridge HiCARS 1 L2 Geolocated Ice Thickness, Version 1 [WWW Document]. Boulder, Color. USA. NASA Natl. Snow Ice Data Cent. Distrib. Act. Arch. Cent.

Brook, D., 1972. Stratigraphy of the Theron Mountains. Br. Antarct. Surv. Bull. 29, 67–89.

Chaput, J., Aster, R. C., Huerta, A., Sun, X., Lloyd, A., Wiens, D., et al. (2014). The crustal thickness of West Antarctica. *Journal of Geophysical Research: Solid Earth*, *119*, 378–395. https://doi.org/10.1002/2013JB010642

Chiappini, M., Ferraccioli, F., Bozzo, E., & Damaske, D. (2002). Regional compilation and analysis of aeromagnetic anomalies for the Transantarctic Mountains-Ross Sea sector of the Antarctic. *Tectonophysics*, *347*, 121–137. https://doi.org/10.1016/S0040-1951(01)00241-4

Collinson, J. W., Isbell, J. L., Elliot, D. H., Miller, M. F., Miller, J. M. G., & Veevers, J. J. (1994). *Permian-Triassic Transantarctic basin*, *Geological Society of America Memoirs* (Vol. 184, pp. 173–222).

Cook, C. P., Van De Flierdt, T., Williams, T., Hemming, S. R., Iwai, M., Kobayashi, M., et al. (2013). Dynamic behaviour of the East Antarctic ice sheet during Pliocene warmth. *Nature Geoscience*, *6*, 765–769. https://doi.org/10.1038/ngeo1889

Damiani, T. M., Jordan, T. A., Ferraccioli, F., Young, D. A., & Blankenship, D. D. (2014). Variable crustal thickness beneath Thwaites Glacier revealed from airborne gravimetry, possible implications for geothermal heat flux in West Antarctica. *Earth and Planetary Science Letters*, *407*, 109–122. https://doi.org/10.1016/j.epsl.2014.09.023

DeConto, R. M., & Pollard, D. (2016). Contribution of Antarctica to past and future sea-level rise. *Nature*, *531*, 591–597. https://doi.org/10.1038/nature17145

Diekmann, B., & Kuhn, G. (1999). Provenance and dispersal of glacial-marine surface sediments in the Weddell Sea and adjoining areas, Antarctica: Ice-rafting versus current transport. *Marine Geology*, *158*, 209–231. https://doi.org/10.1016/S0025-3227(98)00165-0

Diez, A., Matsuoka, K., Ferraccioli, F., Jordan, T. A., Corr, H. F., Kohler, J., et al. (2018). Basal settings control fast ice flow in the Recovery/Slessor/Bailey Region, East Antarctica. *Geophysical Research Letters*, *45*, 2706–2715. https://doi.org/10.1002/2017GL076601

Drewry, D. J. (1983). *Antarctica: Glaciological and geophysical folio*. Scott Polar Research Institute, University of Cambridge.

Ebinger, C. J., Karner, G. D., & Weissel, J. K. (1991). Mechanical strength of extended continental lithosphere: Constraints from the Western Rift System, East Africa. *Tectonics*, *10*, 1239–1256. https://doi.org/10.1029/91TC00579
Elliot, D. H., & Fleming, T. H. (2004). Occurrence and dispersal of magmas in the Jurassic Ferrar Large Igneous Province, Antarctica. *Gondwana Research*, *7*, 223–237. https://doi.org/10.1016/S1342-937X(05)70322-1
Evans, K. R., McKenna, L. W., Lieberman, B. S., Weichert, W. D., & Macleod, K. G. (2018). Geology of the Nelson Limestone, Postel Nunatak, Patuxent Range, Antarctica. *Antarctic Science*, *30*, 29–43. https://doi.org/10.1017/S0954102017000396
Fairhead, J. D., & Okereke, C. S. (1988). Depths to major density contrasts beneath the West African rift system in Nigeria and Camaroon based on the spectral analysis of gravity data. *Journal of African Earth Sciences*, *7*, 769–777.
Ferraccioli, F., Armadillo, E., Jordan, T., Bozzo, E., & Corr, H. (2009). Aeromagnetic exploration over the East Antarctic Ice Sheet: A new view of the Wilkes Subglacial Basin. *Tectonophysics*, *478*, 62–77. https://doi.org/10.1016/j.tecto.2009.03.013
Ferraccioli, F., & Bozzo, E. (1999). Inherited crustal features and tectonic blocks of the Transantarctic Mountains: An aeromagnetic perspective (Victoria Land, Antarctica). *Journal of Geophysical Research*, *104*, 25,297–25,319. https://doi.org/10.1029/1998JB900041
Ferraccioli, F., & Bozzo, E. (2003). Cenozoic strike-slip faulting from the eastern margin of the Wilkes Subglacial Basin to the western margin of the Ross Sea Rift: an aeromagnetic connection. *Geological Society, London, Special Publications*, *210*, 109–133. https://doi.org/10.1144/GSL.SP.2003.210.01.07
Ferraccioli, F., Finn, C. A., Jordan, T. A., Bell, R. E., Anderson, L. M., & Damaske, D. (2011). East Antarctic rifting triggers uplift of the Gamburtsev Mountains. *Nature*, *479*, 388–392. https://doi.org/10.1038/nature10566
Ferraccioli, F., Jones, P. C., Curtis, M. L., Leat, P. T., & Riley, T. R. (2005). Tectonic and magmatic patterns in the Jutulstraumen rift (?) region, East Antarctica, as imaged by high-resolution aeromagnetic data. *Earth, Planets and Space*, *57*, 767–780.
Ferris, J., Johnson, A., & Storey, B. (1998). Form and extent of the Dufek intrusion, Antarctica, from newly compiled aeromagnetic data. *Earth and Planetary Science Letters*, *154*, 185–202. https://doi.org/10.1016/S0012-821X(97)00165-9
Ferris, J. K., Storey, B. C., Vaughan, A. P. M., Kyle, P. R., & Jones, P. C. (2003). The Dufek and Forrestal intrusions, Antarctica: A centre for Ferrar Large Igneous Province dike emplacement? *Geophysical Research Letters*, *30*(6), 1648. https://doi.org/10.1029/2002GL016719
Forsberg, R., Olesen, A. V., Ferraccioli, F., Jordan, T. A., Matsuoka, K., Zakrajsek, A., et al. (2018). Exploring the Recovery Lakes region and interior Dronning Maud Land, East Antarctica, with airborne gravity, magnetic and radar measurements. *Geological Society, London, Special Publications*, *461*. https://doi.org/10.1144/SP461.17
Frederick, B. C., Young, D. A., Blankenship, D. D., Richter, T. G., Kempf, S. D., Ferraccioli, F., & Siegert, M. J. (2016). Distribution of subglacial sediments across the Wilkes Subglacial Basin, East Antarctica. *Journal of Geophysical Research: Earth Surface*, *121*, 351–371. https://doi.org/10.1002/2015JF003760
Fretwell, P., Pritchard, H. D., Vaughan, D. G., Bamber, J. L., Barrand, N. E., Bell, R., et al. (2013). Bedmap2: Improved ice bed, surface and thickness datasets for Antarctica. *Cryosphere*, *7*, 375–393. https://doi.org/10.5194/tc-7-375-2013
Gasson, E., DeConto, R. M., & Pollard, D. (2015). Antarctic bedrock topography uncertainty and ice sheet stability. *Geophysical Research Letters*, *42*, 5372–5377. https://doi.org/10.1002/2015GL064322
Golledge, N. R., Kowalewski, D. E., Naish, T. R., Levy, R. H., Fogwill, C. J., & Gasson, E. G. W. (2015). The multi-millennial Antarctic commitment to future sea-level rise. *Nature*, *526*, 421–425. https://doi.org/10.1038/nature15706
Golledge, N. R., Levy, R. H., McKay, R. M., & Naish, T. R. (2017). East Antarctic ice sheet most vulnerable to Weddell Sea warming. *Geophysical Research Letters*, *44*, 2343–2351. https://doi.org/10.1002/2016GL072422
Golynsky, A. V., Ferraccioli, F., Hong, J. K., Golynsky, D. A., von Frese, R. R. B., Young, D. A., et al. (2018). New Magnetic Anomaly Map of the Antarctic. *Geophysical Research Letters*, *45*, 6437–6449. https://doi.org/10.1029/2018GL078153
Goodge, J. W., & Finn, C. A. (2010). Glimpses of East Antarctica: Aeromagnetic and satellite magnetic view from the central transantarctic mountains of East Antarctica. *Journal of Geophysical Research*, 115, B09103. https://doi.org/10.1029/2009JB006890
Hellmer, H. H., Kauker, F., Timmermann, R., Determann, J., & Rae, J. (2012). Twenty-first-century warming of a large Antarctic ice-shelf cavity by a redirected coastal current. *Nature*, *485*, 225–228. https://doi.org/10.1038/nature11064
Humbert, A., Steinhage, D., Helm, V., Beyer, S., & Kleiner, T. (2018). Missing Evidence of Widespread Subglacial Lakes at Recovery Glacier, Antarctica. *Journal of Geophysical Research: Earth Surface*, *123*, 2802–2826. https://doi.org/10.1029/2017JF004591
Jamieson, S. S. R., Stokes, C. R., Ross, N., Rippin, D. M., Bingham, R. G., Wilson, D. S., et al. (2014). The glacial geomorphology of the Antarctic ice sheet bed. *Antarctic Science*, *26*, 724–741. https://doi.org/10.1017/S0954102014000212
Jeofry, H., Ross, N., Corr, H. F. J., Li, J., Morlighem, M., Gogineni, P., & Siegert, M. J. (2018). A new bed elevation model for the Weddell Sea sector of the West Antarctic Ice Sheet. *Earth System Science Data*, *10*, 711–725. https://doi.org/10.5194/essd-10-711-2018
Jordan, T. A., Ferraccioli, F., & Leat, P. T. (2017). New geophysical compilations link crustal block motion to Jurassic extension and strike-slip faulting in the Weddell Sea Rift System of West Antarctica. *Gondwana Research*, *42*, 29–48. https://doi.org/10.1016/j.gr.2016.09.009
Jordan, T. A., Ferraccioli, F., Ross, N., Corr, H. F. J., Leat, P. T., Bingham, R. G., et al. (2013). Inland extent of the Weddell Sea Rift imaged by new aerogeophysical data. *Tectonophysics*, *585*, 137–160. https://doi.org/10.1016/j.tecto.2012.09.010
Jordan, T. A., Martin, C., Ferraccioli, F., Matsuoka, K., Corr, H., Forsberg, R., et al. (2018). Anomalously high geothermal flux near the South Pole. *Scientific Reports*, *8*(1). https://doi.org/10.1038/s41598-018-35182-0
Karner, G. D., Studinger, M., & Bell, R. E. (2005). Gravity anomalies of sedimentary basins and their mechanical implications: Application to the Ross Sea basins, West Antarctica. *Earth and Planetary Science Letters*, *235*, 577–596. https://doi.org/10.1016/j.epsl.2005.04.016
Karner, G. D., & Watts, A. B. (1983). Gravity anomalies and flexure of the lithosphere at mountain ranges. *Journal of Geophysical Research*, *88*, 10,449–10,477.
Krohne, N., Lisker, F., Kleinschmidt, G., Klugel, A., Laufer, A., Estrada, S., & Spiegel, C. (2016). The Shackleton Range (East Antarctica): An alien block at the rim of Gondwana? *Geological Magazine*, *155*(4), 841–864. https://doi.org/10.1017/S0016756816001011
Ku, C. C., & Sharp, J. A. (1983). Werner deconvolution for automated magnetic interpretation and its refinement using Marquardt's inverse modeling. *Geophysics*, *48*, 754–774. https://doi.org/10.1190/1.1441505
Langley, K., Tinto, K., Block, A., Bell, R. E., Kohler, J., & Scambos, T. (2014). Onset of fast flow in Recovery Ice Stream, East Antarctica: A comparison of potential causes. *Journal of Glaciology*, *60*, 1–8. https://doi.org/10.3189/2014JoG14J063
Leinweber, V. T., & Jokat, W. (2012). The Jurassic history of the Africa-Antarctica corridor—New constraints from magnetic data on the conjugate continental margins. *Tectonophysics*, *530*, 87–101. https://doi.org/10.1016/j.tecto.2011.11.008
Leuschen, C., Gogineni, P., Rodriguez-Morales, F., Paden, J., Allen, C., 2016. IceBridge MCoRDS L2 ice thickness, version 1. Boulder, Color. USA. NASA Natl. Snow Ice Data Cent. Distrib. Act. Arch. Cent.
Lisker, F., & Läufer, A. L. (2013). The Mesozoic Victoria Basin: Vanished link between Antarctica and Australia. *Geology*, *41*, 1043–1046. https://doi.org/10.1130/G33409.1

Lisker, F., Prenzel, J., Läufer, A. L., & Spiegel, C. (2014). Recent thermochronological research in Northern Victoria Land, Antarctica. *Polarforschung*, *84*, 59–66.

Lough, A. C., Wiens, D. A., & Nyblade, A. (2018). Reactivation of ancient Antarctic rift zones by intraplate seismicity. *Nature Geoscience*, *11*(7), 515–519. https://doi.org/10.1038/s41561-018-0140-6

Maritati, A., Aitken, A. R. A., Young, D. A., Roberts, J. L., Blankenship, D. D., & Siegert, M. J. (2016). The tectonic development and erosion of the Knox Subglacial Sedimentary Basin, East Antarctica. *Geophysical Research Letters*, *43*, 10,728–10,737. https://doi.org/10.1002/2016GL071063

McGregor, V.R., Wade, F.A., 1969. Geology of the Western Queen Maud Mountains. Am. Geogr. Soc. Map Folio Ser. 12.

Mengel, M., & Levermann, A. (2014). Ice plug prevents irreversible discharge from East Antarctica. *Nature Climate Change*, *4*, 451–455. https://doi.org/10.1038/nclimate2226

Mercer, J. H. (1978). West Antarctic ice sheet and CO_2 greenhouse effect: a threat of disaster. *Nature*, *271*, 321–325. https://doi.org/10.1073/pnas.0703993104

Mirsky, A., 1969. Geology of the Ohio Range-Liv glacier area. Am. Geogr. Soc. Map Folio Ser. 12.

Parker, R. L. (1972). The rapid calculation of potential anomalies. *Geophysical Journal International*, *31*, 447–455. https://doi.org/10.1111/j.1365-246X.1973.tb06513.x

Paxman, G. J. G., Jamieson, S. S. R., Ferraccioli, F., Bentley, M. J., Forsberg, R., Ross, N., et al. (2017). Uplift and tilting of the Shackleton Range in East Antarctica driven by glacial erosion and normal faulting. *Journal of Geophysical Research: Solid Earth*, *122*, 2390–2408. https://doi.org/10.1002/2016JB013841

Paxman, G. J. G., Jamieson, S. S. R., Ferraccioli, F., Bentley, M. J., Ross, N., Armadillo, E., et al. (2018). Bedrock erosion surfaces record former East Antarctic Ice Sheet extent. *Geophysical Research Letters*, *45*, 4114–4123. https://doi.org/10.1029/2018GL077268

Paxman, G. J. G., Watts, A. B., Ferraccioli, F., Jordan, T. A., Bell, R. E., Jamieson, S. S. R., & Finn, C. A. (2016). Erosion-driven uplift in the Gamburtsev Subglacial Mountains of East Antarctica. *Earth and Planetary Science Letters*, *452*, 1–14. https://doi.org/10.1016/j.epsl.2016.07.040

Pollard, D., DeConto, R. M., & Alley, R. B. (2015). Potential Antarctic Ice Sheet retreat driven by hydrofracturing and ice cliff failure. *Earth and Planetary Science Letters*, *412*, 112–121. https://doi.org/10.1016/j.epsl.2014.12.035

Prenzel, J., Lisker, F., Monsees, N., Balestrieri, M. L., Läufer, A., & Spiegel, C. (2018). Development and inversion of the Mesozoic Victoria Basin in the Terra Nova Bay (Transantarctic Mountains) derived from thermochronological data. *Gondwana Research*, *53*, 110–128. https://doi.org/10.1016/j.gr.2017.04.025

Reese, R., Gudmundsson, G. H., Levermann, A., & Winkelmann, R. (2018). The far reach of ice-shelf thinning in Antarctica. *Nature Climate Change*, *8*, 53–57. https://doi.org/10.1038/s41558-017-0020-x

Rignot, E., Mouginot, J., & Scheuchl, B. (2011). Ice flow of the Antarctic ice sheet. *Science*, *333*, 1427–1430. https://doi.org/10.1126/science.1208336

Rippin, D. M., Bingham, R. G., Jordan, T. A., Wright, A. P., Ross, N., Corr, H. F. J., et al. (2014). Basal roughness of the Institute and Möller Ice Streams, West Antarctica: Process determination and landscape interpretation. *Geomorphology*, *214*, 139–147. https://doi.org/10.1016/j.geomorph.2014.01.021

Ross, N., Bingham, R. G., Corr, H. F. J., Ferraccioli, F., Jordan, T. A., Le Brocq, A. M., et al. (2012). Steep reverse bed slope at the grounding line of the Weddell Sea sector in West Antarctica. *Nature Geoscience*, *5*, 393–396. https://doi.org/10.1038/ngeo1468

Roy, M., van de Flierdt, T., Hemming, S. R., & Goldstein, S. L. (2007). 40Ar/39Ar ages of hornblende grains and bulk Sm/Nd isotopes of circum-Antarctic glacio-marine sediments: Implications for sediment provenance in the southern ocean. *Chemical Geology*, *244*, 507–519. https://doi.org/10.1016/j.chemgeo.2007.07.017

Scambos, T. A., Bohlander, J. A., Shuman, C. A., & Skvarca, P. (2004). Glacier acceleration and thinning after ice shelf collapse in the Larsen B embayment, Antarctica. *Geophysical Research Letters*, *31*, L18402. https://doi.org/10.1029/2004GL020670

Scheinert, M., Ferraccioli, F., Schwabe, J., Bell, R., Studinger, M., Damaske, D., et al. (2016). New Antarctic gravity anomaly grid for enhanced geodetic and geophysical studies in Antarctica. *Geophysical Research Letters*, *43*, 600–610. https://doi.org/10.1002/2015GL067439

Schmidt, D.L., Ford, A.B., 1969. Geology of the Pensacola and Thiel Mountains. Am. Geogr. Soc. Map Folio Ser. 12.

Schoof, C. (2003). The effect of basal topography on ice sheet dynamics. Contin. Mech. *Thermodyn*, *15*, 295–307. https://doi.org/10.1007/s00161-003-0119-3

Shepherd, T., Bamber, J. L., & Ferraccioli, F. (2006). Subglacial geology in Coats Land, East Antarctica, revealed by airborne magnetics and radar sounding. *Earth and Planetary Science Letters*, *244*, 323–335. https://doi.org/10.1016/j.epsl.2006.01.068

Slater, T., Shepherd, A., McMillan, M., Muir, A., Gilbert, L., Hogg, A. E., et al. (2018). A new Digital Elevation Model of Antarctica derived from CryoSat-2 altimetry. *Cryosphere*, *12*, 1551–1562. https://doi.org/10.5194/tc-2017-223

Smith, B. E., Fricker, H. A., Joughin, I. R., & Tulaczyk, S. (2009). An inventory of active subglacial lakes in Antarctica detected by ICESat (2003-2008). *Journal of Glaciology*, *55*, 573–595. https://doi.org/10.3189/002214309789470879

Storey, B. C., Macdonald, D. I. M., Dalziel, I. W. D., Isbell, J. L., & Millar, I. L. (1996). Early Paleozoic sedimentation, magmatism, and deformation in the Pensacola Mountains, Antarctica: The significance of the Ross orogeny. *Geological Society of America Bulletin*, *108*, 685–707. https://doi.org/10.1130/0016-7606(1996)108<0685:EPSMAD>2.3.CO;2

Studinger, M., Bell, R. E., Blankenship, D. D., Finn, C. A., Arko, R. A., Morse, D. L., & Joughin, I. (2001). Subglacial sediments: A regional geological template for ice flow in West Antarctica. *Geophysical Research Letters*, *28*, 3493–3496. https://doi.org/10.1029/2000GL011788

Studinger, M., Bell, R. E., Buck, W. R., Karner, G. D., & Blankenship, D. D. (2004). Sub-ice geology inland of the Transantarctic Mountains in light of new aerogeophysical data. *Earth and Planetary Science Letters*, *220*, 391–408. https://doi.org/10.1016/S0012-821X(04)00066-4

Studinger, M., Bell, R. E., Fitzgerald, P. G., & Buck, W. R. (2006). Crustal architecture of the Transantarctic Mountains between the Scott and Reedy Glacier region and South Pole from aerogeophysical data. *Earth and Planetary Science Letters*, *250*, 182–199. https://doi.org/10.1016/j.epsl.2006.07.035

Studinger, M., & Miller, H. (1999). Crustal structure of the Filchner-Ronne Shelf and Coats Land, Antarctica, from gravity and magnetic data: Implications for the breakup of Gondwana. *Journal of Geophysical Research*, *104*, 20,379–20,394. https://doi.org/10.1029/1999JB900117

Stump, E. (1995). *The Ross orogen of the Transantarctic Mountains*. New York, NY, USA: Cambridge University Press.

Tessensohn, F., Kleinschmidt, G., Talarico, F., Buggisch, W., Brommer, A., Henjes-Kunst, F., et al. (1999). Ross-Age amalgamation of east and west Gondwana: Evidence from the Shackleton Range. *Terra Antarctica*, *6*, 317–325.

Thomas, R. H. (1979). The dynamics of marine ice sheets. *Journal of Glaciology*, *24*, 167–177.

Walter, H. J., Hegner, E., Diekmann, B., Kuhn, G., & van der Loeff Rutgers, M. M. (2000). Provenance and transport of terrigenous sediment in the South Atlantic Ocean and their relations to glacial and interglacial cycles: Nd and Sr isotopic evidence. *Geochimica et Cosmochimica Acta*, *64*, 3813–3827. https://doi.org/10.1016/S0016-7037(00)00476-2

Wannamaker, P. E., Stodt, J. A., Pellerin, L., Olsen, S. L., & Hall, D. B. (2004). Structure and thermal regime beneath the South Pole region, East Antarctica, from magnetotelluric measurements. *Geophysical Journal International*, *157*, 36–54. https://doi.org/10.1111/j.1365-246X.2004.02156.x

Watts, A. B., & Moore, J. D. P. (2017). Flexural isostasy: Constraints from gravity and topography power spectra. *Journal Geophysical Research: Solid Earth*, *122*, 1–14. https://doi.org/10.1002/2017JB014571

Wessel, P., Smith, W. H. F., Scharroo, R., Luis, J., & Wobbe, F. (2013). Generic Mapping Tools: Improved version released. *Eos, Transactions American Geophysical Union*, *94*, 409–410. https://doi.org/10.1002/2013EO450001

Winberry, J. P., & Anandakrishnan, S. (2004). Crustal structure of the West Antarctic rift system and Marie Byrd Land hotspot. *Geology*, *32*, 977–980. https://doi.org/10.1130/G20768.1

Winsborrow, M. C. M., Clark, C. D., & Stokes, C. R. (2010). What controls the location of ice streams? *Earth-Science Reviews*, *103*, 45–59. https://doi.org/10.1016/j.earscirev.2010.07.003

Winter, K., Ross, N., Ferraccioli, F., Jordan, T. A., Corr, H. F. J., Forsberg, R., et al. (2018). Topographic steering of enhanced ice flow at the bottleneck between East and West Antarctica. *Geophysical Research Letters*, *45*, 1–9. https://doi.org/10.1029/2018GL077504

Young, D. A., Wright, A. P., Roberts, J. L., Warner, R. C., Young, N. W., Greenbaum, J. S., et al. (2011). A dynamic early East Antarctic Ice Sheet suggested by ice-covered fjord landscapes. *Nature*, *474*, 72–75. https://doi.org/10.1038/nature10114